# Motor neurons are dispensable for the assembly of a sensorimotor circuit for gaze stabilization

**Dena Goldblatt**,[1,2] **Başak Rosti**,[1] **Kyla R. Hamling**,[1] **Paige Leary**,[1] **Harsh Panchal**,[1] **Marlyn Li**,[1,2] **Hannah Gelnaw**,[1] **Stephanie Huang**,[1,2] **Cheryl Quainoo**,[1] **David Schoppik**[1,3,*]
[1] Depts. of Otolaryngology, Neuroscience & Physiology, and the Neuroscience Institute, NYU Langone Health
[2] Center for Neural Science, New York University
[3] Lead Contact
[*] Correspondence: schoppik@gmail.com

**Sensorimotor reflex circuits engage distinct neuronal subtypes, defined by precise connectivity, to transform sensation into compensatory behavior. Whether and how motor neuron populations specify the subtype fate and/or sensory connectivity of their pre-motor partners remains controversial. Here, we discovered that motor neurons are dispensable for proper connectivity in the vestibular reflex circuit that stabilizes gaze. We first measured activity following vestibular sensation in pre-motor projection neurons after constitutive loss of their extraocular motor neuron partners. We observed normal responses and topography indicative of unchanged functional connectivity between sensory neurons and projection neurons. Next, we show that projection neurons remain anatomically and molecularly poised to connect appropriately with their downstream partners. Lastly, we show that the transcriptional signatures that typify projection neurons develop independently of motor partners. Our findings comprehensively overturn a long-standing model: that connectivity in the circuit for gaze stabilization is retrogradely determined by motor partner-derived signals. By defining the contribution of motor neurons to specification of an archetypal sensorimotor circuit, our work speaks to comparable processes in the spinal cord and advances our understanding of principles of neural development.**

## INTRODUCTION

Developing sensorimotor reflex circuits must precisely connect functional subtypes of neurons to ensure appropriate behavior. For example, withdrawal from noxious stimuli requires maturation of a sensorimotor circuit that uses subtypes of spinal interneurons to transform noxious stimulation into activation of both ipsilateral flexor and contralateral extensor motor neurons [1]. Work over the past 40 years has highlighted motor partner populations as possible orchestrators of connectivity in pre-motor reflex circuits [2–6], but controversy remains about the nature of their role. In the spinal cord, molecular perturbations of motor neuron identity have provided evidence both for [7–11] and against [12–16] an instructive role in establishing connectivity. Part of this controversy stems from the wide variety of inputs to spinal motor neurons [17], the molecular and functional heterogeneity of pre-motor interneurons [14,15], and their complex roles in gait and posture [18]. Further, transcription factors play multivariate and redundant roles in spinal motor neuron development [19,20], such that the effects of molecular perturbations of identity can be masked.

The sensorimotor circuit for vertical gaze stabilization offers a simple framework to evaluate whether and how motor neurons shape pre-motor circuit fate and connectivity. The vertebrate vestibulo-ocular reflex circuit consists of three neuron types – peripheral sensory, central projection, and extraocular motor neurons – that stabilize gaze after head/body tilts (Figure 1A) [21]. Subtype fate, anatomical connectivity, and function are inextricably linked: directionally-tuned sensory neurons innervate nose-up/nose-down subtypes of projection neurons, which in turn innervate specific motor neurons that selectively control either eyes-down or eyes-up muscles [3,22–29]. As both the recipients and origin of directional information, projection neuron fate specification is paramount to proper circuit assembly. Recent work has established the vertical vestibulo-ocular reflex circuit in zebrafish as a model to uncover determinants of fate and connectivity [24–26,29] given the ease of optical imaging, abundant tools for genetic perturbations, rapid development, and robust evolutionary conservation.

The current model for vestibulo-ocular reflex circuit development was motivated by pioneering work in chick [3,30] and formalized by Hans Straka: "[circuit assembly] is accomplished by a specification process that retrogradely transmits post-synaptic target identities to pre-synaptic neurons." [31]. In its strongest form, this "retrograde" model posits a causal role for extraocular motor neurons in specifying the fate (sensory selectivity) of central projection neurons. This key prediction – that loss of motor neurons would disrupt

sensory selectivity in pre-synaptic projection neurons – remains untested. In zebrafish, extraocular motor neurons are temporally poised for such a role. Motor neurons are organized into spatial pools, and though synaptogenesis at ocular muscle targets begins late in development[32], motor neuron fate (muscle target and pool location) is determined early[33]. Projection neurons are born at roughly the same time as motor neurons and extend axons shortly afterwards, poising them to receive deterministic signals that could retrogradely specify their sensory selectivity[29].

Here, we adopted a loss-of-function approach to determine whether motor partner populations specify identity or instruct connectivity across an entire vestibular reflex circuit in zebrafish. We generated a new mutant allele for the *phox2a* gene to eliminate the extraocular motor neurons used for vertical gaze stabilization. Combining functional, anatomical, and sequencing approaches, we then demonstrated that motor neurons are dispensable for three aspects of pre-motor reflex circuit assembly: (i) directionally-appropriate connectivity between sensory and projection neurons, (ii) assembly of projection neurons with motor partners, and (iii) the transcriptional profiles of projection neurons. The current model of vestibulo-ocular reflex circuit development must therefore be revised: up/down projection neuron subtype fate cannot be retrogradely established by a motor partner-derived signal. Instead, the signals that specify fate must lie elsewhere. More broadly, our work argues against a deterministic role of motor neurons in specifying the fate and sensory connectivity of pre-motor circuit components.

## RESULTS

### Constitutive loss of *phox2a* prevents extraocular motor neuron specification and impairs vertical gaze stabilization behavior

Extraocular motor neurons for vertical/torsional gaze stabilization are located in cranial nuclei III (nIII) and IV (nIV). To eliminate nIII/nIV motor neurons and by extension, any secreted signals, we used a genetic loss-of-function approach (Figure 1A). A single highly-conserved transcription factor, *phoxa*, specifies nIII/nIV fate[34–37]. In the vestibulo-ocular reflex circuit, *phox2a* is exclusively expressed in nIII/nIV motor neurons but not its upstream partners (Figure 1B). Therefore, *phox2a* is an ideal genetic target to eliminate motor-derived signals without compromising evaluations of upstream functional development.

Prior mutagenesis established a *phox2a* loss-of-function allele in zebrafish[34], but the line has since been lost. Here, we generated three new *phox2a* loss-of-function alleles using CRISPR/Cas9 mutagenesis (Figure 1C) (one allele shown here; additional alleles described in Methods). Consistent with prior reports and human mutations[38], both eyes in *phox2a* null mutants were exotropic (rotated towards the ears) reflecting a loss of motor neurons in nIII/nIV. *phox2a* mutants failed to hatch from their chorions without manual intervention and did not inflate their swim bladders by 5 days post-fertilization (dpf) (Figure 1D), phenotypes not previously reported[34]. Consequently, null mutants do not survive past 7 dpf. We did not observe these morphological phenotypes in wildtype and heterozygous siblings (Figure 1D). As vestibulo-ocular reflex circuit architecture and behavior is established by 5 dpf[24,25,29], premature lethality did not preclude further measurements of circuit development.

To validate *phox2a* loss-of-function, we leveraged a downstream transcription factor: *isl1*[39]. The *Tg(isl1:GFP)* line[40] labels all nIII/nIV motor neurons except inferior oblique neurons[33], which comprise one of four pools for upwards eye rotations. We first quantified changes in the number of labeled nIII/nIV neurons (Figure 1E-Figure 1F). In *phox2a* mutants, we observed an expected and near-total loss of *isl1* expression (WT: 298±19 neurons across both hemispheres; null: 19±11 neurons; Wilcoxon rank sum test, $p=2.5\times10^{-4}$) at 5 dpf, well-after nIII/nIV differentiation is complete[33]. As a secondary measure of nIII/nIV motor neuron fate, we performed fluorescent *in situ* hybridization against *vachta*, a marker of cholinergic motor neurons, when differentiation is complete at 2 dpf. Unlike sibling controls, nIII/nIV neurons in *phox2a* mutants failed to express *vachta*, validating that loss of *phox2a* perturbs at least two key transcriptional markers of nIII/nIV fate (Figure S1). Unexpectedly, we also observed slightly fewer neurons in *phox2a* heterozygotes (heterozygote: 229±20 neurons; Wilcoxon rank sum test against WT, $p=6.7\times10^{-4}$). In heterozygotes, loss of *isl1* fluorescence was restricted to the medial domain of dorsal nIII, which contains some of the earliest-born neurons in nIII/nIV (Figure S2A-Figure S2C)[33]. Globally, this manifested as a rostral and ventral shift in the positions of all neurons mapped (Figure S2D) (two-sample, two-tailed KS test, WT vs. heterozygotes: mediolateral axis, $p=0.13$; rostrocaudal: $p=4.0\times10^{-29}$; dorsoventral: $p=2.5\times10^{-9}$). This region contains two motor pools that control the inferior (IR) and medial rectus (MR) muscles[33]. We conclude

that *phox2a* acts in a dose- and birthdate-dependent manner to specify nIII motor pool fate.

Together, these observations validate our *phox2a* loss of function alleles as a selective means to disrupt nIII/nIV motor neuron fate specification and vertical eye rotation behavior.

## Peripheral-to-central circuit assembly does not require motor partners

Vertical gaze stabilization requires that (1) peripheral VIII$^{th}$ nerve sensory afferents relay tilt sensation (nose-up/nose-down) directly to projection neurons in the tangential nucleus, and (2) projection neurons innervate appropriate nIII/nIV pools (eyes-up/eyes-down). For proper circuit function, appropriate connectivity must first develop across up/down circuit subtypes. The "retrograde" model predicts that motor partners specify circuit assembly. Therefore, in the absence of motor neurons, projection neurons should fail to respond selectively to directional tilt sensations – either due to loss of their fate, the fate of upstream sensory afferents, or sensory-to-central connectivity.

To evaluate upstream circuit formation, we measured tilt-evoked responses in projection neurons using Tilt-In-Place Microscopy (TIPM)[41] (Figure 2A-Figure 2B). Peripherally, tilts activate utricular VIII$^{th}$ nerve sensory inputs to projection neurons[29,41]. We used a galvanometer to deliver tonic nose-up and nose-down pitch tilts to *phox2a* null larvae and sibling controls. We then measured the activity of a calcium indicator, GCaMP6s[42], in projection neurons. We performed experiments at 5 dpf, when nearly all projection neurons are selective for one tilt direction[29], circuit architecture is stable[25], and gaze stabilization behavior is directionally-appropriate[24].

Projection neuron responses and topography were strikingly unchanged in *phox2a* mutants compared to controls. There was no change in the number of projection neurons observed across N=5 sibling controls and *phox2a* mutants (mean control number: 42±4 neurons per hemisphere; mean in *phox2a* mutants: 39±3 neurons; two-tailed Wilcoxon rank sum test, p=0.22). We next recorded the activity of n=297 neurons from N=16 *phox2a* mutants and n=440 neurons from N=21 sibling controls (Methods and Table 1 split by genotype). We observed comparable ratios of projection neuron subtypes (sib: 46% nose-down, 47% nose-up, 7% untuned; *phox2a*: 49% nose-down, 44% nose-up, 7% untuned) (Figure 2C). Next, we evaluated their topography (Figure 2D-Figure 2E). Projection neurons are topographically organized along the dorso-ventral axis by their directional selectivity[29]. Global spatial separation between subtypes remained significant in *phox2a* mutants (one-way multivariate analysis of variance, p=0.004). We also compared the topography of nose-up and nose-down neurons separately across *phox2a* genotypes (Methods and Table 2 split by genotype). Nose-down neurons were comparably distributed between null and control larvae (one-way multivariate analysis of variance, p=0.15). We observed a minor lateral shift to nose-up neurons in null mutants (median mediolateral position, sib: 15.2μm from medial edge; *phox2a*, 13.2μm; two-tailed, two-sample KS test, $p=3.0\times10^{-4}$) but no changes in other spatial axes (dorsoventral: p=0.16; rostrocaudal: p=0.56). The small medial deviation (2μm across a 40μm space) is within the limits of our registration error. We conclude that projection neuron topography is established independently of motor partners.

Projection neuron sensitivity and selectivity also developed comparably between *phox2a* mutants and siblings (Figure 2F-Figure 2K). Projection neurons responded to tilt sensations with comparable magnitudes (Figure 2G-Figure 2J) (nose-down mean ΔF/F, sib: 1.86±1.69; *phox2a*: 2.07±1.48; two-tailed Wilcoxon rank sum test, p=0.98; nose-up mean ΔF/F, sib: 1.24±1.23; *phox2a*: 1.02±0.89; p=0.18). Previously, we defined a metric to describe a neuron's selectivity for one tilt direction (0 = equal responses to up/down; 1 = maximally selective)[29]. Directional selectivity remained unchanged in *phox2a* mutants (Figure 2H-Figure 2K) (nose-down mean index, sib: 0.73±0.29; *phox2a*: 0.68±0.29; two-tailed Wilcoxon rank sum test, p=0.85; nose-up mean index, sib: 0.85±0.26; *phox2a*: 0.81±0.29; p=0.12). Collectively, this demonstrates that the functional responses of projection neurons and, by inference, connectivity with utricular afferents are not shaped by motor partners.

Ventral projection neurons receive additional input from the semicircular canals[29], which encode phasic (fast) tilt sensation. To activate sensory afferents from the semicircular canals, we used TIPM to deliver two impulses of angular rotation (Figure 3A-Figure 3B)[29,41]. We observed no changes in *phox2a* mutants (Table 1 and Table 2 for genotype splits). Projection neurons responded to impulses in comparable ratios (Figure 3E) (sib: 58% responsive; *phox2a*: 71% responsive). Responsive projection neu-

rons remained localized to the ventral nucleus (dorsoventral axis: two-tailed, two-sample KS test, p=0.99). We observed minor positional changes in the rostrocaudal and mediolateral axes (Table 2), which are not topographically organized by impulse responsivity[29]; this deviation is again within our margin of registration error. Lastly, the functional properties of projection neurons were unchanged (Figure 3F-Figure 3G). We observed no change in calcium response magnitudes (Figure 3F) (mean $\Delta F/F$, sib: 0.33±0.29; *phox2a*: 0.36±0.40; two-tailed Wilcoxon rank sum test, p=0.85) or lack of directional selectivity (Figure 3G) (mean index, sib: 0.07±0.41; *phox2a*: 0.06±0.40; p=0.39). Therefore, fate and connectivity between phasic sensory afferents and projection neurons must not require motor partners.

Lastly, we considered whether loss of one subtype of nIII/nIV neurons might alter connectivity. For example, loss of eyes-down motor pools could impair wiring between their corresponding nose-up sensory and projection neuron partners. Here, we leveraged *phox2a* heterozygotes, which lack a subtype of nIII neurons (IR/MR) that contribute to downwards eye rotations (Figure S2). We observed no differences in tonic tilt responses between *phox2a* wildtype, heterozygote, and null larvae, though we did note a minor decrease in response strength to impulses (statistics in Table 1). We note that *phox2a* heterozygotes do not lack all motor pools for downwards eye rotations. Nevertheless, we conclude that individual motor pools do not meaningfully contribute to connectivity between sensory and projection neurons.

Taken together, these experiments demonstrate intact directional selectivity for two peripheral sensory inputs – utricular and semicircular canal VIII$^{th}$ nerve afferents – and appropriate connectivity with projection neurons. We conclude that functional sensory-to-central circuit formation is established independently of motor partners.

## Projection neurons remain competent to assemble with appropriate motor targets

Motor partners could secrete signals that initiate pre-motor axon outgrowth, target arriving axons to specific motor pools, or trigger synaptogenesis[3]. Motor pool topography in nIII/nIV reflects ocular muscle targets: dorsal pools innervate downward-rotating muscles (superior oblique and inferior rectus), while ventral pools target the converse (eyes-up, superior rectus and inferior oblique)[33,43]. In turn, projection neuron somatic and axonal organization mirrors motor pool topography[28,29], which could facilitate directionally-selective circuit assembly. We reasoned that projection neurons may fail to initiate axon outgrowth, target spatially-appropriate motor pools, and/or form synapses in *phox2a* mutants. To test this hypothesis, we measured changes in projection neuron anatomy at 5 dpf, when axonal arbors are established and stable[25].

To test whether projection neurons establish gross, long-range (hindbrain to midbrain) axonal outgrowths, we performed optical retrograde labeling[44] using a photolabile protein, Kaede. We targeted the medial longitudinal fasciculus at the midbrain-hindbrain boundary, which contains projection neuron axons[25,29] (Figure 4A). In both *phox2a* mutants and sibling controls, we observed retrograde photolabeling of projection neuron soma (Figure 4B), supporting that initial axon outgrowth does not require motor partner-derived signals.

Next, we evaluated whether projection neuron axons remain capable of wiring with spatially-appropriate motor partners. Projection neuron axons segregate along the dorsal (nose-up) and ventral (nose-down) axes according to their birth order (early/late born, respectively)[28,29] and the pool topography of their motor targets[33]. To test whether projection neurons retain this topography, we optically labeled the axons of early-born (before 30 hpf) projection neurons[29]. In *phox2a* mutants, axons remained dorsoventrally segregated at midbrain targets (Figure 4C, inset). Typically, projection neurons robustly collateralize to nIII/nIV targets at the midbrain-hindbrain boundary. We did not observe collaterals to nIII/nIV in *phox2a* mutants (Figure 4C). However, projection neurons still robustly arborized to more rostral, spinal-projecting targets in the nucleus of the medial longitudinal fasciculus, suggesting they retain the machinery necessary to collateralize. Consistent with this hypothesis, we observed that projection neurons formed occasional, small collaterals in *phox2a* mutants with few (1-5%) nIII/nIV neurons remaining (Figure 4D). We conclude that projection neurons remain competent to assemble with spatially-appropriate targets.

If motor neurons are required to initiate synaptogenesis, then projection neurons should fail to develop pre-synaptic machinery. To test this hypothesis, we performed fluorescent *in situ* hybridization against common pre-synaptic transcripts: synaptophysin a

(*sypa*), synaptic vesicle glycoprotein (*sv2*), and synapsin I (*syn1*). In both *phox2a* mutants and controls, we observed robust transcript expression in projection neuron somata at 5 dpf (Figure 4E), well-after synaptogenesis onset in wildtype larvae[29]. Motor partner-derived signals are thus not required for projection neurons to develop the necessary components for synaptogenesis.

Though motor neurons may play later roles in selecting and/or refining pre-motor input specificity, our data supports that projection neurons remain anatomically and molecularly poised to assemble with appropriate targets. We predict that absent collaterals and synapses reflect a lack of adhesive contact necessary to stabilize[45,46], but not instruct the formation of nascent structures.

### The transcriptional profiles of projection neurons are intact in the absence of motor partners

We found that functional and anatomical connectivity, from peripheral sensors to motor targets, develop independently of motor partners. Fate in the vestibulo-ocular reflex circuit follows from connectivity[21], but neuronal fate can also be defined with respect to unique transcriptional signatures. Previously, we developed a sequencing pipeline to discover transcription factors that specify functional subtypes of spinal motor neurons and evaluate the consequences of perturbations on transcriptional fate[47]. We adapted this approach to determine if loss of motor-derived signals changed the transcriptional profiles of projection neurons.

We compared the transcriptional profiles of projection neurons in *phox2a* mutants and sibling controls (Figure 5A) using bulk RNA sequencing. Sibling controls included both wildtype and heterozygous *phox2a* larvae (Figure S2). We performed sequencing experiments at 72 hours post-fertilization (hpf), after projection neuron differentiation is complete and synaptogenesis to motor targets has peaked[29]. We sequenced projection neurons labeled by *Tg(-6.7Tru.Hcrtr2:GAL4-VP16);Tg(UAS-E1b:Kaede)*[24,25,48,49] (Methods, Figure 5B, Figure S3). Neurons labeled in this line include, but are not exclusive to the projection neurons in the tangential nucleus used for vertical gaze stabilization. Therefore, we evaluated our bulk RNA sequencing dataset in the context of a single-cell reference atlas derived from the same transgenic line (Methods, Figure S4) to minimize noise from other labeled populations. We used *evx2*[50] as a reference, as it was expressed in all projection neurons (Figure S4D) and highly detected (36%) in singly-profiled projection neurons.

There were strikingly few differentially-expressed genes in projection neurons between *phox2a* siblings and null mutants (Figure 5C, Table 3). All candidate differentially-expressed genes were lowly-expressed (detected in <10% of reference projection neurons, Figure 5D). To determine if any candidates were differentially expressed in projection neurons, we used a fluorescent *in situ* hybridization method[51] in which fluorescence intensity correlates with detected transcript expression reliably across individual larvae (Figure S5). We evaluated 8 candidate genes (Figure 5E-Figure 5F); four with the highest detection levels in projection neurons (*satb1a*, *rxfp2a*, *mapk6*, and *p4hb*), two with high significance and fold change thresholds (*itga9*, *twf1b*), and two highly-detected controls (*evx2*, *myt1la*). Qualitatively, we observed no differences in expression patterns between *phox2a* mutants and siblings.

We considered that our inability to detect differentially-expressed genes could arise from our exclusion of candidates based on their expression in our reference single-cell atlas. Therefore, we repeated our analyses in unfiltered bulk sequencing data. The top 50 highest-expressed genes in *phox2a* siblings were highly detected in singly-profiled neurons labeled by *Tg(-6.7Tru.Hcrtr2:GAL4-VP16);Tg(UAS-E1b:Kaede)*, including projection neurons (Table 4) (mean detection in projection neurons: 55%±21%, min=0%, max=87%). This suggests that our dissections adequately captured our target population. However, we again identified few differentially-expressed genes in our unfiltered data (Figure S6A-Figure S6C), with substantial decreases as significance stringency increased. *In situ* hybridization validated that top candidates remained lowly expressed in projection neurons in both *phox2a* siblings and mutants (Figure S6D), Importantly, nearly all candidates had low detection across all neurons in our reference single-cell atlas and had predicted expression in populations such as glia and the caudal hindbrain (Methods, Table 5). Notably, some candidates were highly expressed in a subset of medial vestibular nucleus neurons, which lies on the medial edge of the tangential nucleus and expressed *phox2a* (Methods, Figure S7, and Table 6). Together, we conclude that any differential gene expression in our data either reflects noise or contamination from other labeled populations, but not projection neurons in the tangential nucleus.

We acknowledge the possibility that our *in situ* method is insufficiently quantitative to detect subtle differences in expression. Similarly, despite using both bulk and single-cell RNA sequencing approaches, we may lack the resolution to uncover differential gene

expression within projection neurons, particularly given the inclusion of heterozygous *phox2a* siblings in controls. Nevertheless, consistent with functional and anatomical characterization, our sequencing data argues that projection neurons acquire the correct transcriptional profiles in the absence of motor partner-derived signals. Our findings are reminiscent of recent reports that the molecular signatures of spinal interneurons develop independently of motor partners [15].

## DISCUSSION

Here, we show that motor neurons are dispensable for fate specification in a canonical sensorimotor circuit. We first demonstrated that peripheral sensory and central projection neurons develop appropriate, directionally-selective connectivity and topography independently of their motor partners. Next, we established that projection neurons remain anatomically and molecularly competent to assemble with motor partners. Lastly, we show that loss of motor neurons does not meaningfully alter the transcriptional signatures of their pre-motor projection neuron partners. By providing causal evidence against an instructional role of motor partners for sensory connectivity, our work forces a revision of the current model for vestibulo-ocular reflex circuit formation. As proper connectivity across multiple synapses is foundational for proper function, our work speaks to mechanisms responsible for sensorimotor circuit assembly.

### Transcriptional influences on motor neuron fate specification

While the primary focus of our work was circuit assembly, we found that, unexpectedly, *phox2a* acts in a dose-dependent manner to specify extraocular motor pool fate. Key evidence comes from *phox2a* heterozygotes, in which the earliest-born dorsal neurons in nIII are lost but later-born neurons in nIII/nIV are intact. This observation extends prior characterizations of *phox2a* mutations in zebrafish [34], chick [36], and human [37,38]. Prior work hypothesized that *phox2a* dosage may regulate midbrain motor neuron differentiation into visceral and somatic types [36]. In other systems, transcription [52–54], growth [55] and axon guidance factors [56] can act in such a graded manner to regulate coarse cell type specification and wiring specificity. We extend these ideas to show that *phox2a* dose-dependency acts both over closely-related subtypes (pools within a single cranial nucleus) and along a temporal axis, where partial dosage preferentially targets the earliest-born neurons [33]. Specifically, if *phox2a* is expressed in neural progenitor cells that give rise to nIII/nIV, then the earliest-born motor neurons would have the shortest exposure to *phox2a*.

Molecular insight into ocular motor neuron pool specification is sparse but would be welcome given the strong links between genetic development and ocular motor disease [38,57–59]. For example, subpopulation markers could resolve the topography of pools within dorsal nIII; whether IR/MR pools are spatially segregated or intermingled [33,60]; whether the medial/lateral axis reflects functional differences among motor neuron subtypes; and whether/how local interactions between motor neuron pools contributes to fate specification [61]. In spinal circuits, the rich molecular understanding of motor pool specification [47,62–65] has enabled targeted perturbations of pool identity, allowing for major discoveries of their roles in circuit assembly [9,13,15,66]. Our findings thus represent a step forward towards understanding how developmental deficits may contribute to ocular motor disorders [67].

### Motor neurons: active or passive architects of pre-motor connectivity?

Our discoveries advance outstanding controversies over whether motor neurons actively or passively shape pre-motor connectivity. We find that extraocular motor neuron axons do not serve as "pioneers" [68–72], with pre-motor axon targeting following passively from motor-derived pathfinding signals [2]. Such a model predicts that projection neuron targeting would be entirely ablated after constitutive loss of extraocular motor neurons and their secreted signals [73–77]. Instead, we observed that projection neurons still establish long-range (hindbrain to midbrain) axonal projections, with appropriate spatial segregation that matches the topography of their motor partners [28,29,33]. Our findings complement reports in spinal circuits that pre-motor targeting is grossly appropriate after manipulating the spatial source of, but not ablating, potential pathfinding signals [13], and that the transcriptional fate of pre-motor projection neurons similarly develops independently [15]. We point to the late development of ocular musculature [78,79] compared to spinal musculature [2] as a potential source of the dispensability of muscle-derived signals.

Our work is also inconsistent with the strongest form of the "retrograde" hypothesis for vestibulo-ocular reflex circuit assembly. Originally, the retrograde model posited that motor neurons release a diffusable or cell-surface available signal that instructs pre-

motor collaterals to sprout and then innervate specific pools, enabling behavioral specificity[3,31]. Here, the proper spatial and temporal segregation of projection neuron axons suggests they remain poised to wire with spatially-appropriate (dorsal/ventral pools) targets. Additional evidence comes from incomplete *phox2a* knockouts (1-5% of nIII/nIV remaining), where projection neurons still form collaterals, though not robustly or reliably. We predict that projection neuron axons do not require a target-derived cue to grow, search, and synapse onto motor targets, and simply lack the adhesive contact necessary to stabilize nascent structures (reviewed in[45,46]).

Nevertheless, extraocular motor neurons might still play an active or passive role in selecting and/or refining input specificity from their projection neuron partners. In spinal circuits, motor pool position passively imposes geometric constrains on pre-motor axon targeting[13,14], and manipulating the dendritic structure of motor neuron axons transforms input specificity[9,11]. Genetic perturbations of nIII/nIV motor neuron position selectively compromise ocular responses to directional visual stimuli[61], though the circuit-level origin of such impairments is unclear. For the vestibulo-ocular reflex circuit, transforming all motor pools to the same fate or genetically "scrambling" pool position could resolve whether motor input specificity is truly hard-wired in projection neurons, or whether projection neurons instead target gross spatial domains irrespective of partner identity[13]. Motor neuron-derived signals are of course capable of shaping their input by strengthening/weakening their inputs. Importantly, our results suggest that such signals will not define the fate of projection neurons, and by extension, circuit architecture.

We note that our study does not eliminate one additional source of post-synaptic partner signals to projection neurons. As in primates[80], projection neurons also contact neurons in the interstitial nucleus of Cajal, also known as the nucleus of the medial longitudinal fasciculus (INC/nMLF)[24]. INC/nMLF neurons project early in development[81] to spinal circuits used for postural stabilization during swimming[82–86]. Notably, ablation of projection neurons disrupts postural stability[50]. As we did not observe postural deficits in *phox2a* mutants, we infer that projection neuron connectivity to INC/nMLF targets is present and functional. Correspondingly, the development of projection neuron collaterals and synapses to INC/nMLF neurons appeared qualitatively normal in *phox2a* mutants, supporting our interpretation that projection neurons retain the capacity to properly assemble with post-synaptic targets even though similar structures to extraocular motor neurons are absent. In the future, if a similarly specific marker like *phox2a* is identified that labels the INC/nMLF, it will be possible to test whether these neurons play a role in vestibulo-ocular reflex circuit development.

### Alternative mechanisms for fate specification and sensory input specificity in projection neurons

What is the origin of signals that govern projection neuron fate and sensory input specificity, if not motor-derived? In comparable systems, fate signals can be intrinsically-expressed or originate from extrinsic sources. For example, intrinsic genetic mechanisms assemble laminar connectivity in visual circuits[87,88] and facilitate sensorimotor matching in spinal circuits[9,89–91]. In directionally-selective retinal circuits, subtype fate is established in a similar manner[92,93]. In "intrinsic" models, synaptic specificity arises from molecular matching between subtypes[94–96]. Alternatively, in somatosensory and auditory circuits, transcriptional fate depends on extrinsic signals such as growth factors[97] and sensation[98], respectively. In spinal circuits, positional fate, which constrains connectivity[13], is established by extrinsic codes such as morphogen gradients in early development[99] and Hox factors[63,64]. In "extrinsic" models, early inputs are often erroneous and refined by activity[100,101] or molecular factors[102]. Collectively, these findings offer two alternative models for how vestibulo-ocular reflex circuit assembly emerges.

The tight links between birth order, somatic position, and stimulus selectivity[28,29,33,85,103,104] across vestibulo-ocular reflex circuit populations support an "intrinsic" determination model. Further, neurogenesis and initial axon targeting develops contemporaneously for sensory afferents[55,103,105,106], projection neurons[3,29,107–109], and extraocular motor neurons[3,33,39,110–112], suggesting that neurons are poised to assemble with targets as early as their time of differentiation. Importantly, an "intrinsic specification" model makes a testable prediction about how and when sensory selectivity should emerge across the circuit: projection neurons and extraocular motor neurons should be directionally selective as soon as pre-synaptic input is established. Such evidence would justify future molecular inquiries into the underlying genetic factors, expanding early characterizations of the mechanisms that shape hindbrain topography[113,114], recent molecular profiling of the zebrafish hindbrain[115,116], and reports of molecular match-

ing between extraocular motor neurons and muscle[117,118]. Operationally, the present study lays a foundation for molecular explorations of projection neuron subtype determinants by establishing bulk- and single-cell transcriptomic profiling and *in situ* validation pipelines.

Conversely, evidence that stimulus selectivity emerges gradually would suggest that sensory afferents and/or projection neurons initially wire indiscriminately and that circuit connectivity is refined in time by extrinsic forces. Prior work in the vestibulo-ocular reflex circuit has proposed developmental roles for sensory-derived trophic factors[119] and activity-dependent refinement[120,121], though sensory afferents develop typically in the absence of utricular input[122] and ocular motor behavior does not depend on stimulus-driven activity[123]. Here, an "extrinsic" determination model would predict that connectivity is established by an anterogradely-transmitted signal – that is, from sensory afferents to ocular muscles. If so, then future investigations might constitutively ablate sensory afferents to eliminate activity-driven, diffusible, or cell-surface instructional signals, similar to the present study. The directional bias in opsin-evoked activity in projection neurons[25], together with their transcriptional profiles established here, offer a clear readout of the role of sensory-derived factors. However, genetic targets exclusive to vestibular sensory afferents for gaze stabilization have not been identified, and tissue-specific genetic ablations remain limited in zebrafish. Looking ahead, resolving when and how stimulus selectivity emerges across the vestibulo-ocular reflex circuit will be key to understanding whether connectivity with pre- and/or post-synaptic partners instructs subtype fate, or whether subtype fate instructs connectivity.

## Conclusion

Here, we discovered that motor partners do not determine pre-motor fate and sensory connectivity for the projection neurons that stabilize gaze. Our results overturn the current model that stimulus selectivity and connectivity are retrogradely specified, a major step towards understanding the origin, and eventually nature, of mechanisms that assemble an archetypal sensorimotor reflex circuit. Instead, our data support and extend recent models in spinal systems that motor partners do not actively construct sensory-to-interneuron reflex circuit architecture, but may later refine their inputs. By defining the contribution of motor neurons to specification and sensory connectivity of gaze-stabilizing central projection neurons, our work speaks to principles of sensorimotor circuit assembly.

# MATERIALS AND METHODS

## RESOURCE AVAILABILITY

### Lead Contact

Further information and requests for resources and reagents should be directed to and will be fulfilled by the lead contact, David Schoppik (schoppik@gmail.com).

### Materials Availability

Mutant fish lines generated in this study will be deposited to the Zebrafish International Resource Center (ZIRC).

### Data and code availability

- All data and code are deposited at the Open Science Framework and are publicly available at DOI: 10.17605/OSF.IO/93V6E

## EXPERIMENTAL MODEL AND SUBJECT DETAILS

### Fish care

All protocols and procedures involving zebrafish were approved by the New York University Langone School of Medicine Institutional Animal Care & Use Committee (IACUC). All larvae were raised at 28.5°C at a density of 20-50 larvae in 25-40 ml of buffered E3 (1mM HEPES added). Larvae used for photofill experiments were raised in constant darkness; all other fish were raised on a standard 14/10h light/dark cycle. Larvae for experiments were between 3-5 days post-fertilization (dpf).

## Transgenic lines

Experiments were conducted on the *mifta*$^{-/-}$ background to remove pigment. All experiments used larvae from the F3 generation or older of a newly-created line of *phox2a* mutants (described below) on the following backgrounds: *Tg(isl1:GFP)*[40] to validate *phox2a* loss-of-function; *Tg(isl1:GFP);Tg(-6.7Tru.Hcrtr2:GAL4-VP16)*[25,49] to drive UAS reporter expression; *Tg(UAS-E1b:Kaede)*[48] for anatomical imaging experiments; and *Tg(UAS:GCaMP6s)*[83] for calcium imaging experiments. All larvae were selected for brightness of fluorescence relative to siblings. Mendelian ratios were observed, supporting that selected larvae were homozygous for fluorescent reporter alleles.

## Generation of *phox2a* mutants

*phox2a* mutant lines were generated using CRISPR/Cas9 mutagenesis. Two guide RNAs (gRNAs) were designed using the Benchling CRISPR Guide RNA Design Tool (see: key resources, Table 7). gRNAs were located towards the 5' region of exon 1 to minimize the size of any translated protein. gRNAs were incubated with Cas9 protein before co-injection into *Tg(isl1:GFP)* embryos at the single cell stage. Injected embryos were screened for anatomical phenotypes (reduction in *isl1*-positive nIII/nIV motor neurons). Phenotypic embryos (F0) and their embryos were raised and genotyped via sequencing to identify and validate germline mutations. Three founders were identified and used for experiments: (1) *phox2a*$^{d22}$ has a 22 bp deletion from base pairs 249 to 270, (2) *phox2a*$^{d19}$ has a 19 bp deletion from base pairs 262 to 280, and (3) *phox2a*$^{i2}$ has a 2 bp insertion (AG) from base pairs 261 to 262. Each mutation created a nonsense mutation, causing a predicted premature stop codon at the beginning of the homeobox. All alleles were validated using complementation assays, and larvae from all three alleles were used in experiments. For brevity, only one allele (*phox2a*$^{d22}$) is shown in Figure 1.

## Maintenance of *phox2a* adults

*phox2a* null larvae do not survive past 7 dpf. Sibling embryos (*phox2a*$^{+/+}$ or *phox2a*$^{+/-}$) were raised and genotyped to identify heterozygotes for line propagation. Primers for genotyping are listed in the Key Resources table (Table 7). Genomic DNA was amplified using a polymerase (DreamTaq PCR Master Mix 2X, Thermo Fisher Scientific K1071), 60°annealing temperature, 30 second elongation time, and 35 cycles of PCR. PCR generates a 169 bp product (wildtype), 147 bp product (*phox2a*$^{d22}$), 150 bp product (*phox2a*$^{d19}$), or 171 bp product (*phox2a*$^{i2}$). *phox2a*$^{d22}$ and *phox2a*$^{d19}$ DNA was evaluated using gel electrophoresis; *phox2a*$^{i2}$ was assessed via sequencing with the reverse primer (Genewiz, Azenta Life Sciences, South Plainfield, New Jersey).

# METHOD DETAILS

## Confocal imaging

Larvae were anesthetized in 0.2 mg/mL ethyl-3-aminobenzoic acid ethyl ester (MESAB, Sigma-Aldrich E10521, St. Louis, MO) prior to confocal imaging except where noted. Larvae were mounted dorsal side-up (axial view) or lateral side-up (sagittal view) in 2% low-melting point agarose (Thermo Fisher Scientific 16520) in E3. Images were collected on a Zeiss LSM800 confocal microscope with a 20x water-immersion objective (Zeiss W Plan-Apochromat 20x/1.0). Images of tangential nucleus soma and axons were acquired in a lateral mount with an 80x80 µm imaging window. Stacks spanned ~30-40 µm, sampled every 1 µm. Images of nIII/nIV motor neurons were acquired in a dorsal mount with a 213x106 µm imaging window; stacks spanned approximately 90 µm, sampled every 1.5 µm. Images to validate nIII/nIV expression in a lateral mount were acquired using a 319x319 µm imaging window. Raw image stacks were analyzed using Fiji/ImageJ[124].

## Identification of *phox2a* larvae

Prior to experiments, larvae were designated as *phox2a* mutants or sibling (wildtype/heterozygote) controls based on two criteria: gross loss of *Tg(isl1:GFP)* fluorescence in nIII/nIV at 2 dpf, visualized using a SugarCube LED Illuminator (Ushio America, Cypress CA) on a stereomicroscope (Leica Microsystems, Wetzlar, Germany) and absence of a swim bladder at 5 dpf. For anatomical and calcium imaging experiments, allele designations were validated using confocal imaging of nIII/nIV motor neurons: total or near-total loss of nIII/nIV neurons (null), selective loss of IR/MR neurons (heterozygote), or normal expression (wildtype). Designations were

confirmed after experiments using genotyping. For RNA sequencing and fluorescent *in situ* experiments, sibling controls (wild-type/heterozygote) were combined.

### Birthdating of nIII/nIV motor neurons

Early-born neurons in nIII/nIV were optically tagged using *in vivo* birthdating [29,33,125] on *Tg(isl1:Kaede)*$^{ch103}$ larvae [126]. Briefly, whole embryos were exposed to UV light for five minutes at experimenter-defined timepoints and subsequently raised in darkness to prevent background conversion. At 5 dpf, larvae were imaged on a confocal microscope. Neurons born before the time of photo-conversion expressed red, converted Kaede; neurons born after expressed only green, unconverted Kaede.

### Fluorescent *in situ* hybridization and imaging

Experiments were performed using Hybridization Chain Reaction (HCR) for whole-mount zebrafish larvae [51,127]. Probes were generated using the HCR 3.0 probe maker [128] using the sense sequence of the canonical gene cDNA from NCBI. All larvae were from the *Tg(isl1:GFP);Tg(-6.7Tru.Hcrtr2:GAL4-VP16);Tg(UAS-E1b:Kaede)* background. Larvae were pre-identified as null mutants or siblings (wildtype or heterozygotes) and combined in equal ratios (8-10 larvae per condition, 16-20 larvae total) into a single 5 mL centrifuge tube for fixation and HCR. Larvae were fixed overnight with 4% PFA in PBS at 4° C and stored in 100% methanol at -20° C. Subsequently, HCR was performed as described in [127], with adjustments to proteinase K incubation time based on age (2 dpf: 23 min incubation; 3 dpf: 30 min incubation; 5 dpf: 35 min incubation). HCR experiments used buffers and amplifiers from Molecular Instruments (Los Angeles, CA). DAPI staining was performed on some samples at 1:2000 from 5mg/ml stock solution, incubated overnight at 4° C. Samples were stored in 1x PBS at 4° C and imaged on a confocal microscope within four days. Prior to imaging, larvae were re-screened for *Tg(isl1:GFP)* fluorescence to identify null mutants and sibling controls. For each probe, imaging parameters were determined using a sibling control and kept constant for all subsequent larvae. Comparable settings (within 1% laser power) were used across probes.

### Calcium imaging of tonic and impulse tilt stimuli responses

Experiments were performed as described in [29] using Tilt-In-Place Microscopy [41]. All experiments used 5 dpf larvae from the *Tg(isl1:GFP);(Tg(-6.7Tru.Hcrtr2:GAL4-VP16);Tg(UAS:GCaMP6s)* background. Briefly, larvae were mounted dorsal-up in 2% low-melt agarose in E3 onto a large beam diameter galvanometer system (ThorLabs GVS011). Tonic pitch-tilt stimuli were presented over a 65-second period in the following order: horizontal baseline (5 sec at 0°), nose-down tilt (15 sec at -19°), horizontal imaging (15 sec at 0°), nose-up tilt (15 sec at 19°), and horizontal imaging (15 sec at 0°). Impulse stimuli contained a 4 msec eccentric rotation, a 2 msec hold, and a 4 msec restoration step to horizontal and were presented twice over a 65-second imaging window: horizontal baseline (20 sec), impulse (10 msec), horizontal imaging (30 sec), impulse (10 msec), horizontal imaging (15 sec). Tonic and impulse stimuli were presented in alternating sets (impulse, then tonic) with a total of three stimulus set repeats.

Imaging was performed using a 20x water immersion objective (Olympus XLUMPLFLN20xW 20x/1.0), an infrared laser (Spectra-Physics MaiTai HP) at 920nm using 6.1-18.8 mW of power at the sample, and ThorLabs LS 3.0 software. Experiments were conducted in the dark. High-resolution anatomy scans of nIII/nIV motor neurons were performed for each experiment to validate allele designations. Scans used a 147x147 µm imaging window, a 90 µm stack sampled every 1.5 µm, and a 5.2 microsecond pixel dwell time. Anatomy scans of the tangential nucleus were acquired using a 148x91 µm imaging window as a 40-50 µm stack sampled every 1 µm. For stimulus imaging, the tangential nucleus was sampled every 3-6 µm based on cell density. 6-10 planes were sampled for each hemisphere. Ventral planes were imaged at higher magnification (112x68 µm imaging window) than dorsal planes (148x91 µm window) to avoid photomultiplier tube saturation from in-frame GFP fluorescence; magnification was corrected for in later analyses. Laser power was adjusted for each sampled plane due to the light scattering properties of zebrafish tissue. As greater power was required for ventral planes, imaging was always performed from ventral to dorsal to minimize photobleaching effects. Stimulus imaging was performed at 3 frames/second (2.2 µs pixel dwell time) with a total time of approximately two hours per fish.

The number of neurons sampled per fish for each genotype are as follows (n=mean/standard deviation per fish; total cells/total fish): (1) Wildtype reference dataset: n=22±14 neurons/fish, N=255/10 total; (2) *phox2a*$^{+/+}$: 33±13 neurons/fish, N=76/5 total; (3)

410 *phox2a*$^{+/-}$: 43±9 neurons/fish, N=109/6 total; (4) *phox2a*$^{-/-}$: 35±14neurons/fish, N=297/16 total.

411 **Retrograde photolabeling of tangential nucleus neurons**

412 Experiments were performed as described in [29] based on [44] on 5 dpf larvae from the *Tg(isl1:GFP);Tg(-6.7Tru.Hcrtr2:GAL4-*
413 *VP16);Tg(UAS-E1b:Kaede)* background. Briefly, experiments leveraged a photoconvertible protein, Kaede, which irreversibly con-
414 verts from green to red with ultraviolet light. Larvae were raised in darkness to minimize background conversions. Larvae were
415 mounted dorsal-up in 2% agarose under a confocal microscope. An imaging window was centered over the medial longitudinal
416 fasciculus (MLF) and repeatedly scanned with a 405 nm laser for 30 seconds until fully converted (green to red). Off-target photo-
417 conversion was assessed (e.g., conversion of projections lateral to the MLF). Larvae were unmounted, left to recover in E3 for 4 hours
418 in darkness, and then re-mounted in a lateral mount. An imaging window was centered around the tangential nucleus (see: Con-
419 focal Imaging). Retrogradely-labeled soma were identified by their center-surround fluorescence appearance: red converted cyto-
420 plasm surrounding an unconverted green nucleus.

421 **Neuron harvesting, dissociation, and flow cytometry**

422 Experiments were performed on 72-74 hpf larvae from the *Tg(isl1:GFP);Tg(-6.7Tru.Hcrtr2:GAL4-VP16);Tg(UAS-E1b:Kaede)* back-
423 ground. At 2 dpf, larvae were designated as null or sibling (wildtype/heterozygote) as described above. Three experimenters (D.G.,
424 K.R.H., and P.L) harvested neurons in parallel. Larvae were anesthetized in MESAB in Earle's Balanced Salt Solution with calcium,
425 magnesium, and phenol red (EBSS, Thermo Fisher Scientific 24010043) and mounted dorsal-up in 2% agarose. Fluorescence in
426 tangential nucleus neurons was visualized using a SugarCube LED Illuminator (Ushio America, Cypress CA) using 10x eyepieces on
427 a stereomicroscope (Leica Microsystems, Wetzlar, Germany). Neurons were harvested using a thin wall glass capillary tube (4 inch,
428 OD 1.0 MM, World Precision Instruments) into EBSS in a non-stick Eppendorf tube and kept on ice until dissociation.

429 Neurons were dissociated in 20 units/mL of papain prepared in EBSS (Worthington Biochemical), 2000 units/mL of deoxyribonu-
430 cleic prepared in EBSS (Worthington Biochemical), and 100 mg/mL of Type 1A Collagenase (Sigma Aldrich) prepared in Hanks
431 Buffered Salt Solution without calcium/magnesium (HBSS, Thermo Fisher Scientific). Neurons were incubated for 45 minutes at
432 31.5°C with a gentle vortex every 10-15 min, then passed through a 20 µm filter and centrifuged for 10 mins at 300 x g. After re-
433 moving supernatant, neurons were resuspended in L15 (Thermo Fisher Scientific) with 2% fetal bovine serum (Thermo Fisher Sci-
434 entific). Cell health was evaluated using DAPI, applied at 0.5 µg/ml (Invitrogen) and incubated on ice for 30-45 mins prior to flow
435 cytometry.

436 Flow cytometry was performed using a Sony SH800z cell sorter (100 µm nozzle, 20 psi) to isolate single neurons (Figure S3). Three
437 controls were run: (1) non-fluorescent wildtype neurons, (2) non-fluorescent neurons + DAPI, (3) fluorescent (green) neurons from
438 *Tg(isl1:GFP);Tg(-6.7Tru.Hcrtr2:GAL4-VP16);Tg(UAS-E1b:Kaede)* + DAPI. On average, 2% of neurons were DAPI-positive and ex-
439 cluded. Neurons were evaluated for positive (green) fluorescence. Fluorescence was not evaluated to separate *Tg(UAS-E1b:Kaede)*
440 neurons from those labeled by *Tg(isl1:GFP)*. Neurons were sorted into an Eppendorf tube containing 700 µl of lysis buffer (RNAque-
441 ous Micro Total RNA Isolation Kit, Thermo Fisher Scientific) for downstream bulk RNA sequencing.

442 **Bulk RNA sequencing**

443 RNA isolation was performed using an RNAqueous Micro Total RNA Isolation Kit (Thermo Fisher Scientific). RNA concentration and
444 quality (RIN > 8.0) was evaluated using an RNA 6000 Pico Kit and a 2100 Bioanalyzer system (Agilent Technologies, Santa Clara,
445 California). RNA sequencing was performed by the NYU Genome Technology Center. Libraries were prepared using the low-input
446 Clontech SMART-Seq HT with Nxt HT kit (Takara Bio USA) and sequenced using an Illumina NovaSeq 6000 with an S1 100 Cycle
447 Flow Cell (v1.5).

448 **QUANTIFICATION AND STATISTICAL ANALYSIS**

### Cell counting and spatial mapping of nIII/nIV motor neurons

Analysis was performed in Fiji/ImageJ[124] using the Cell Counter plugin. Anatomical stacks of nIII/nIV were subdivided in the dorsoventral axis as described in[33] to facilitate localization. A point ROI was dropped over each neuron in the plane in which the soma was brightest (center). The number of neurons in each dorsoventral plane and their coordinates were recorded. Neuron coordinates were standardized relative to a (0,0) point, defined as one corner of a standard-sized rectangular box centered over the extent of nIII/nIV in a maximum intensity projection. Differences in spatial location across genotypes was evaluated separately for each spatial axis using a two-tailed, two-sample Kolmogorov-Smirnov test. Probability distributions for figures were generated using the mean and standard deviation from bootstrapped data (n=100 iterations) to ensure results were robust to data from single larva.

### Analysis of calcium imaging experiments

Analysis methods are detailed in[29] and summarized briefly here. Regions of Interest (ROIs) were drawn around tangential nucleus neurons for each stimulus plane sampled and adjusted for minor movement (1-2 μm) between trials. Raw fluorescence traces were extracted using Matlab R2020b (MathWorks, Natick, Massachusetts) and normalized by ROI size to account for variation in magnification. A neuron's response to tonic or impulse stimuli was defined as the change in fluorescence in the first second of restoration to horizontal following tilt delivery. Responses were normalized using a baseline period, defined as the mean fluorescence across the initial baseline window (5 sec) preceding the nose-down tilt (nose-down response) or the last 3 sec of the horizontal restoration following nose-down tilt (nose-up response). This was used to generate a $\Delta F/F$ value. A $\Delta F/F$ response was defined as significant if it was greater than two standard deviations above baseline. Directional selectivity was assigned by normalizing the difference in $\Delta F/F$ responses to each tilt by their sum. This generated a scale of values of $\pm 1$ (i.e., positive values represent nose-up selectivity; negative values, nose-down). Some neurons responded to both tilt directions with high similarity; we set a minimum threshold of abs(0.1) to distinguish neurons with a clear directional selectivity from untuned neurons.

### Spatial mapping of tangential nucleus neurons

Analysis methods are detailed in[29] and summarized briefly here. All imaged neurons were manually registered to a reference framework using Adobe Illustrator (2021). Anatomy stacks from all experiments were aligned in the XY (rostrocaudal, mediolateral) axes using established anatomical landmarks (e.g., Mauthner cell body, medial longitudinal fasciculus, otic capsule). For Z-registration (dorsoventral axis), stacks were subdivided into eight sections using landmarks within and around the tangential nucleus (e.g., Mauthner cell body, neuropil). All registered images were verified by two independent observers (D.G. and S.H.). Neurons were localized to one dorsoventral section and a reference circle, representing a cell, was placed in Illustrator. Coordinates for each reference circle were recorded and standardized to an absolute (0,0) point (dorsomedial-most point of the tangential nucleus). Coordinates were imported into Matlab (R2020b) and used to generate a spatial map of imaged neurons.

### Statistical analysis of differences in tilt responses across *phox2a* genotypes

Statistical comparisons of tonic and impulse tilt responses are summarized in Table 1. Analyses used a one-way analysis of variance with multiple comparisons. No significant differences (tonic tilt responses) or small differences (impulse responses) were observed across genotypes. Control data reported in Results and Figure 2-Figure 3 is an aggregate from wildtype, *phox2a*$^{+/+}$, and *phox2a*$^{+/-}$ larvae.

### Alignment, quality control, and differential expression analysis of bulk sequencing data

Initial alignment and analyses were performed by the Applied Bioinformatics Laboratories at the NYU School of Medicine (RRID:SCR_019178). Sequencing data was aligned to the GRCz11 zebrafish reference genome and two fluorescent markers (Kaede, GFP; NCBI). Eight datasets from four experimental repeats were aligned: four from *phox2a* mutants, and four from sibling controls. One experimental repeat had significantly higher variance in the first and second principal components, likely due to poor quality leading to extremely low transcript counts, and was excluded from downstream analyses. Number of cells/larvae sequenced and used in downstream analysis are as follows: Repeat 1, n=532/n=904 cells from N=28/N=28 *phox2a* null/control lar-

vae; Repeat 2, n=802/n=683 cells from N=27/N=26 *phox2a* null/control larvae; Repeat 3, n=1000/n=1007 cells from N=41/N=40 *phox2a* null/control larvae; Repeat 4 (excluded): n=690/n=571 cells from N=33/N=33 *phox2a* null/control larvae Differential gene expression between conditions (*phox2a* mutants vs. sibling controls) was assessed using DESeq2 [129]. Differentially-expressed candidate genes met two criteria: $\log_2$ fold change >|2| and p adjusted < 0.05.

### Filtering of bulk sequencing data using a reference single-cell sequencing dataset

Analyses were performed in R. Detection of markers for motor neurons (*isl1, isl2a, isl2b*) [130,131] and neurons caudal (*hoxd4a*) [113,132] and lateral (*barhl2*) [114] to rhombomeres 4-6 supported that our dataset included other populations. We applied a filter to exclude erroneous gene expression from non-tangential nucleus populations.

Filtering was performed using an existing single-cell atlas of neurons labeled in *Tg(-6.7Tru.Hcrtr2:GAL4-VP16);(Tg(UAS-E1b:Kaede)*, generated with 10x Genomics. The reference atlas was generated from four experimental samples using the harvest, dissociation, and flow cytometry method described above. The sequenced atlas contained 1,468 neurons (Figure S4A-Figure S4B)). Data was analyzed using Seurat v4.0 [133]. Cluster annotation was performed using a combination of fluorescent *in situ* hybridization as described above (Figure S4C-Figure S4E and other data not shown) and published molecular data of the zebrafish hindbrain [113]. n=159 neurons (11%) were validated as excitatory projection neurons from the tangential nucleus.

Genes in the bulk dataset were only included in downstream analyses if they were expressed above threshold percent of reference projection neurons: 1%, 3%, 5%, 10%, 30%, or 50%. The most stringent filter (50%) was set using the transcription factor *evx2*, which is reported to be expressed in all tangential nucleus neurons [50] and was detected in 36% of reference projection neurons. Qualitatively, we found that gene detection with fluorescent *in situ* hybridization scaled with reference filter stringency (Figure S5). Analyses were performed separately for each threshold. The total number of genes included for downstream analyses for each threshold are as follows: 28,807 (no threshold), 11,278 (1% of reference neurons), 8,346 (3%), 6,701 (5%), 4,185 (10%), 1,105 (30%), 384 (50%). We used the following significance thresholds for differential gene expression in filtered datasets: adjusted p value < 0.05 and abs(log2FoldChange) > 2. The number of differentially expressed genes for each threshold was as follows: 100 (no threshold), 23 (1% of reference neurons), 6 (3%), 2 (5%), 0 (10%).

Projection neurons in the tangential nucleus lie in close proximity to the medial vestibular nucleus (3-5 µm) to the medial edge of the tangential nucleus and 10-20 µm dorsal to the rostral/dorsal edge of the tangential nucleus). Some MVN neurons express *phox2a* (Figure S7). Our reference single-cell atlas isolated a small cluster of *phox2a*-expressing neurons in r5-6 that likely originates from this population. To control for the possibility that some differentially expressed genes are localized to the MVN, and not projection neurons, we also evaluated differential gene expression in the *phox2a*-expressing subset of MVN neurons (n=45 neurons, 3% of reference dataset). Data is shown in Figure S7.

### Generation of representative images for fluorescent *in situ* hybridization

Images were generated using Fiji/ImageJ [124]. An anatomical template of the tangential nucleus was generated based on [29]. Briefly, for sagittal view images, a 30-µm stack was centered over the tangential nucleus. For each plane, a region of interest (ROI) was drawn over all cells within the bounds of the tangential nucleus. Transcript expression outside the ROI was masked. Maximum intensity projections were generated. Minimal or no alterations to brightness/contrast were made for probe expression given the correlation between fluorescence intensity and detected transcript [51].

### Additional statistics

Bias and variability in probability distributions were estimated by bootstrapping, or resampling the raw distributions with replacement [134]. Data shown is the mean and standard deviation of 100 bootstrapped distributions. Topography data was evaluated using two-tailed, two-way Kolmogorov-Smirnov tests. Functional responses to tilts (i.e., calcium response strength, directionality index) were evaluated using two-tailed Wilcoxon rank sum tests. Differences in responses across genotypes were analyzed using one-way analysis of variance tests.

## ACKNOWLEDGMENTS

Research was supported by the National Institute on Deafness and Communication Disorders of the National Institutes of Health under award numbers R01DC017489, F31DC020910, and F31DC019554, the National Institute of Neurological Disorders and Stroke under award numbers F99NS129179, T32NS086750, and the National Cancer Institute P30CA016087. The authors would like to thank Hannah Gelnaw for assistance with fish care, and Jeremy Dasen, Claude Desplan, Katherine Nagel, Dan Sanes, along with the members of the Schoppik and Nagel labs for their valuable feedback and discussions. Finally, the authors gratefully acknowledge the late Hans Straka for his generous insights and encouragement throughout.

## AUTHOR CONTRIBUTIONS

Conceptualization: DG and DS, Methodology: DG, BR, KRH, PL, and DS, Investigation: DG, BR, KRH, PL, ML, HP, HG, SH, and CQ, Visualization: DG, Writing: DG, Editing: DS, Funding Acquisition: DG and DS, Supervision: DS.

## AUTHOR COMPETING INTERESTS

The authors declare no competing interests.

## REFERENCES

1. Charles S. Sherrington. *The Integrative Action of the Nervous System*. Yale University Press, 1906.
2. Michael P. Matise and Cynthia Lance-Jones. A critical period for the specification of motor pools in the chick lumbosacral spinal cord. *Development*, 122(2):659669, February 1996.
3. Joel C. Glover. The development of vestibulo-ocular circuitry in the chicken embryo. *Journal of Physiology-Paris*, 97(1):17–25, Jan 2003.
4. Silvia Arber. Motor circuits in action: Specification, connectivity, and function. *Neuron*, 74(6):975–989, jun 2012.
5. Jeremy S Dasen. Master or servant? emerging roles for motor neuron subtypes in the construction and evolution of locomotor circuits. *Current Opinion in Neurobiology*, 42:25–32, feb 2017.
6. David R. Ladle, Eline Pecho-Vrieseling, and Silvia Arber. Assembly of motor circuits in the spinal cord: Driven to function by genetic and experience-dependent mechanisms. *Neuron*, 56(2):270–283, Oct 2007.
7. Timothy A. Machado, Eftychios Pnevmatikakis, Liam Paninski, Thomas M. Jessell, and Andrew Miri. Primacy of flexor locomotor pattern revealed by ancestral reversion of motor neuron identity. *Cell*, 162(2):338350, July 2015.
8. Christopher A. Hinckley, William A. Alaynick, Benjamin W. Gallarda, Marito Hayashi, Kathryn L. Hilde, Shawn P. Driscoll, Joseph D. Dekker, Haley O. Tucker, Tatyana O. Sharpee, and Samuel L. Pfaff. Spinal locomotor circuits develop using hierarchical rules based on motorneuron position and identity. *Neuron*, 87(5):1008–1021, September 2015.
9. Eline Vrieseling and Silvia Arber. Target-induced transcriptional control of dendritic patterning and connectivity in motor neurons by the ETS gene pea3. *Cell*, 127(7):1439–1452, dec 2006.
10. Myungin Baek, Chiara Pivetta, Jeh-Ping Liu, Silvia Arber, and Jeremy S. Dasen. Columnar-intrinsic cues shape premotor input specificity in locomotor circuits. *Cell Reports*, 21(4):867–877, oct 2017.
11. Nikolaos Balaskas, L.F. Abbott, Thomas M. Jessell, and David Ng. Positional strategies for connection specificity and synaptic organization in spinal sensory-motor circuits. *Neuron*, 102(6):1143–1156.e4, June 2019.
12. Guoying Wang and Sheryl A. Scott. The waiting period of sensory and motor axons in early chick hindlimb: Its role in axon pathfinding and neuronal maturation. *The Journal of Neuroscience*, 20(14):53585366, July 2000.
13. Gülşen Sürmeli, Turgay Akay, Gregory C. Ippolito, Philip W. Tucker, and Thomas M. Jessell. Patterns of spinal sensory-motor connectivity prescribed by a dorsoventral positional template. *Cell*, 147(3):653–665, October 2011.
14. Jay B. Bikoff, Mariano I. Gabitto, Andre F. Rivard, Estelle Drobac, Timothy A. Machado, Andrew Miri, Susan Brenner-Morton, Erica Famojure, Carolyn Diaz, Francisco J. Alvarez, George Z. Mentis, and Thomas M. Jessell. Spinal inhibitory interneuron diversity delineates variant motor microcircuits. *Cell*, 165(1):207–219, mar 2016.
15. Lora B. Sweeney, Jay B. Bikoff, Mariano I. Gabitto, Susan Brenner-Morton, Myungin Baek, Jerry H. Yang, Esteban G. Tabak, Jeremy S. Dasen, Christopher R. Kintner, and Thomas M. Jessell. Origin and segmental diversity of spinal inhibitory interneurons. *Neuron*, 97(2):341–355.e3, January 2018.
16. Maggie M Shin, Catarina Catela, and Jeremy Dasen. Intrinsic control of neuronal diversity and synaptic specificity in a proprioceptive circuit. *eLife*, 9, August 2020.
17. Ole Kiehn. Decoding the organization of spinal circuits that control locomotion. *Nature Reviews Neuroscience*, 17(4):224238, March 2016.
18. J. RAMSAY HUNT. The dual nature of the efferent nervous system: A further study of the static and kinetic systems, their function and symptomatology contents. *Archives of Neurology & Psychiatry*, 10(1):37, July 1923.
19. Kamal Sharma, Hui Z Sheng, Karen Lettieri, Hung Li, Alexander Karavanov, Steven Potter, Heiner Westphal, and Samuel L Pfaff. Lim homeodomain factors lhx3 and lhx4 assign subtype identities for motor neurons. *Cell*, 95(6):817828, December 1998.
20. Sarah A. Hutchinson and Judith S. Eisen. Islet1 and islet2 have equivalent abilities to promote motoneuron formation and to specify motoneuron subtype identity. *Development*, 133(11):21372147, June 2006.
21. J. Szentágothai. Pathways and synaptic articulation patterns connecting vestibular receptors and oculomotor nuclei. In *The Oculomotor System*, pages 205–223. Hoeber Medical Division, Harper and Row, 1964.
22. Hans Straka, Robert Baker, and Edwin Gilland. Rhombomeric organization of vestibular pathways in larval frogs. *Journal of Comparative Neurology*, 437(1):42–55, July 2001.
23. Carmen Díaz, Joel C. Glover, Luis Puelles, and Jan G. Bjaalie. The relationship between hodological and cytoarchitectonic organization in the vestibular complex of the 11-day chicken embryo. *The Journal of Comparative Neurology*, 457(1):87–105, February 2003.
24. Isaac H. Bianco, Leung-Hang Ma, David Schoppik, Drew N. Robson, Michael B. Orger, James C. Beck, Jennifer M. Li, Alexander F. Schier, Florian Engert, and Robert Baker. The tangential nucleus controls a gravito-inertial vestibulo-ocular reflex. *Current Biology*, 22(14):1285–1295, Jul 2012.
25. David Schoppik, Isaac H. Bianco, David A. Prober, Adam D. Douglass, Drew N. Robson, Jennifer M.B. Li, Joel S.F. Greenwood, Edward Soucy, Florian Engert, and Alexander F. Schier. Gaze-stabilizing central vestibular neurons project asymmetrically to extraocular motoneuron pools. *The Journal of Neuroscience*, 37(47):11353–11365, sep 2017.
26. Martha W Bagnall and David Schoppik. Development of vestibular behaviors in zebrafish. *Current Opinion in Neurobiology*, 53:83–89, December 2018.
27. Carmen Díaz and Luis Puelles. Segmental analysis of the vestibular nerve and the efferents of the vestibular complex. *The Anatomical Record*, 302(3):472–484, May 2018.
28. Zhikai Liu, David G. C. Hildebrand, Joshua L. Morgan, Yizhen Jia, Nicholas Slimmon, and Martha W. Bagnall. Organization of the gravity-sensing system in zebrafish. *Nature Communications*, 13(1), August 2022.
29. Dena Goldblatt, Stephanie Huang, Marie R. Greaney, Kyla R. Hamling, Venkatakaushik Voleti, Citlali Perez-Campos, Kripa B. Patel, Wenze Li, Elizabeth M.C. Hillman, Martha W. Bagnall, and David Schoppik. Neuronal birthdate reveals topography in a vestibular brainstem circuit for gaze stabilization. *Current Biology*, 33(7):1265–1281.e7, April 2023.
30. Joel C. Glover. Neuroepithelial 'compartments' and the specification of vestibular projections. In *Progress in Brain Research*, pages 3–21. Elsevier, 2000.
31. Hans Straka. Ontogenetic rules and constraints of vestibulo-ocular reflex development. *Current Opinion in Neurobiology*, 20(6):689–695, December 2010.
32. C. Clark, O. Austen, I. Poparic, and S. Guthrie. $\alpha$2-chimaerin regulates a key axon guidance transition during development of the oculomotor projection. *Journal of Neuroscience*, 33(42):16540–16551, Oct 2013.
33. Marie R. Greaney, Ann E. Privorotskiy, Kristen P. D'Elia, and David Schoppik. Extraocular motoneuron pools develop along a dorsoventral axis in zebrafish, *Danio rerio*. *Journal of Comparative Neurology*, 525(1):65–78, jun 2016.
34. Su Guo, Jennifer Brush, Hiroki Teraoka, Audrey Goddard, Stephen W. Wilson, Mary C. Mullins, and Arnon Rosenthal. Development of noradrenergic neurons in the zebrafish hindbrain requires BMP, FGF8, and the homeodomain protein soulless/phox2a. *Neuron*, 24(3):555–566, November 1999.
35. Eva Coppola, Alexandre Pattyn, Sarah C Guthrie, Christo Goridis, and Michèle Studer. Reciprocal gene replacements reveal unique functions for phox2 genes during neural differentiation. *The EMBO Journal*, 24(24):43924403, December 2005.
36. K. B. Hasan, S. Agarwala, and C. W. Ragsdale. PHOX2a regulation of oculomotor complex nucleogenesis. *Development*, 137(7):1205–1213, Mar 2010.
37. Motoi Nakano, Koki Yamada, Jennifer Fain, Emin C. Sener, Carol J. Selleck, Abdulaziz H. Awad, Johan Zwaan, Paul B. Mullaney, Thomas M. Bosley, and Elizabeth C. Engle. Homozygous mutations in arix(phox2a) result in congenital fibrosis of the extraocular muscles type 2. *Nature Genetics*, 29(3):315320, October 2001.
38. Thomas M. Bosley, Darren T. Oystreck, Richard L. Robertson, Abdulaziz al Awad, Khaled Abu-Amero, and Elizabeth C. Engle. Neurological features of congenital fibrosis of the extraocular muscles type 2 with mutations in PHOX2a. *Brain*, 129(9):2363–2374, September 2006.
39. Alfredo Varela-Echavarria, Samuel L. Pfaff, and Sarah Guthrie. Differential expression of LIM homeobox genes among motor neuron subpopulations in the developing chick brain stem. *Molecular and Cellular Neuroscience*, 8(4):242–257, Oct 1996.
40. S. Higashijima, Y. Hotta, and H. Okamoto. Visualization of cranial motor neurons in live transgenic zebrafish expressing green fluorescent protein under the control of the *Islet*-1 promoter/enhancer. *Journal of Neuroscience*, 20(1):206–218, Jan 2000.

41. Kyla R. Hamling, Yunlu Zhu, Franziska Auer, and David Schoppik. Tilt in place microscopy: a simple, low-cost solution to image neural responses to body rotations. *The Journal of Neuroscience*, 43(6):936948, February 2023.
42. Tsai-Wen Chen, Trevor J. Wardill, Yi Sun, Stefan R. Pulver, Sabine L. Renninger, Amy Baohan, Eric R. Schreiter, Rex A. Kerr, Michael B. Orger, Vivek Jayaraman, Loren L. Looger, Karel Svoboda, and Douglas S. Kim. Ultrasensitive fluorescent proteins for imaging neuronal activity. *Nature*, 499(7458):295–300, July 2013.
43. Craig Evinger. Extraocular motor nuclei: location, morphology and afferents. *Reviews of Oculomotor Research*, 2:81–117, 1988.
44. Avinash Pujala and Minoru Koyama. Chronology-based architecture of descending circuits that underlie the development of locomotor repertoire after birth. *eLife*, 8, February 2019.
45. Matthew B. Dalva, Andrew C. McClelland, and Matthew S. Kayser. Cell adhesion molecules: signalling functions at the synapse. *Nature Reviews Neuroscience*, 8(3):206220, February 2007.
46. Trevor Moreland and Fabienne E. Poulain. To stick or not to stick: The multiple roles of cell adhesion molecules in neural circuit assembly. *Frontiers in Neuroscience*, 16, April 2022.
47. Kristen P. DElia, Hanna Hameedy, Dena Goldblatt, Paul Frazel, Mercer Kriese, Yunlu Zhu, Kyla R. Hamling, Koichi Kawakami, Shane A. Liddelow, David Schoppik, and Jeremy S. Dasen. Determinants of motor neuron functional subtypes important for locomotor speed. *Cell Reports*, 42(9):113049, September 2023.
48. Ethan K. Scott, Lindsay Mason, Aristides B. Arrenberg, Limor Ziv, Nathan J Gosse, Tong Xiao, Neil C. Chi, Kazuhide Asakawa, Koichi Kawakami, and Herwig Baier. Targeting neural circuitry in zebrafish using GAL4 enhancer trapping. *Nature Methods*, mar 2007.
49. Alix M.B. Lacoste, David Schoppik, Drew N. Robson, Martin Haesemeyer, Ruben Portugues, Jennifer M. Li, Owen Randlett, Caroline L. Wee, Florian Engert, and Alexander F. Schier. A convergent and essential interneuron pathway for mauthner-cell-mediated escapes. *Current Biology*, 25(11):1526–1534, jun 2015.
50. Takumi Sugioka, Masashi Tanimoto, and Shin-ichi Higashijima. Biomechanics and neural circuits for vestibular-induced fine postural control in larval zebrafish. *Nature Communications*, 14(1), March 2023.
51. Harry M. T. Choi, Maayan Schwarzkopf, Mark E. Fornace, Aneesh Acharya, Georgios Artavanis, Johannes Stegmaier, Alexandre Cunha, and Niles A. Pierce. Third-generation in situ hybridization chain reaction: multiplexed, quantitative, sensitive, versatile, robust. *Development*, 145(12), June 2018.
52. Rodney P. DeKoter and Harinder Singh. Regulation of b lymphocyte and macrophage development by graded expression of pu.1. *Science*, 288(5470):14391441, May 2000.
53. Zijing Liu, Xuemei Hu, Jun Cai, Ben Liu, Xiaozhong Peng, Michael Wegner, and Mengsheng Qiu. Induction of oligodendrocyte differentiation by olig2 and sox10: Evidence for reciprocal interactions and dosage-dependent mechanisms. *Developmental Biology*, 302(2):683693, February 2007.
54. Stephen N. Sansom, Dean S. Griffiths, Andrea Faedo, Dirk-Jan Kleinjan, Youlin Ruan, James Smith, Veronica van Heyningen, John L. Rubenstein, and Frederick J. Livesey. The level of the transcription factor pax6 is essential for controlling the balance between neural stem cell self-renewal and neurogenesis. *PLoS Genetics*, 5(6):e1000511, June 2009.
55. Shruti Vemaraju, Husniye Kantarci, Mahesh S. Padanad, and Bruce B. Riley. A spatial and temporal gradient of fgf differentially regulates distinct stages of neural development in the zebrafish inner ear. *PLoS Genetics*, 8(11):e1003068, November 2012.
56. Takaki Komiyama, Lora B. Sweeney, Oren Schuldiner, K. Christopher Garcia, and Liqun Luo. Graded expression of semaphorin-1a cell-autonomously directs dendritic targeting of olfactory projection neurons. *Cell*, 128(2):399410, January 2007.
57. Jong G. Park, Max A. Tischfield, Alicia A. Nugent, Long Cheng, Silvio Alessandro Di Gioia, Wai-Man Chan, Gail Maconachie, Thomas M. Bosley, C. Gail Summers, David G. Hunter, Caroline D. Robson, Irene Gottlob, and Elizabeth C. Engle. Loss of mafb function in humans and mice causes duane syndrome, aberrant extraocular muscle innervation, and inner-ear defects. *The American Journal of Human Genetics*, 98(6):12201227, June 2016.
58. Long Cheng, Jigar Desai, CarlosăJ. Miranda, JeremyăS. Duncan, Weihong Qiu, AliciaăA. Nugent, AdrianneăL. Kolpak, CarrieăC. Wu, Eugene Drokhlyansky, MichelleăM. Delisle, Wai-Man Chan, Yan Wei, Friedrich Propst, SamaraăL. Reck-Peterson, Bernd Fritzsch, and ElizabethăC. Engle. Human cfeom1 mutations attenuate kif21a autoinhibition and cause oculomotor axon stalling. *Neuron*, 82(2):334349, April 2014.
59. Gustav Y. Cederquist, Anna Luchniak, Max A. Tischfield, Maya Peeva, Yuyu Song, Manoj P. Menezes, Wai-Man Chan, Caroline Andrews, Sheena Chew, Robyn V. Jamieson, Lavier Gomes, Maree Flaherty, Patricia Ellen Grant, Mohan L. Gupta, and Elizabeth C. Engle. An inherited tubb2b mutation alters a kinesin-binding site and causes polymicrogyria, cfeom and axon dysinnervation. *Human Molecular Genetics*, 21(26):54845499, September 2012.
60. Craig Evinger, Werner M. Graf, and Robert Baker. Extra- and intracellular HRP analysis of the organization of extraocular motoneurons and internuclear neurons in the guinea pig and rabbit. *The Journal of Comparative Neurology*, 262(3):429–445, Aug 1987.
61. Athene Knüfer, Giovanni Diana, Gregory S Walsh, Jonathan DW Clarke, and Sarah Guthrie. Cadherins regulate nuclear topography and function of developing ocular motor circuitry. *eLife*, 9, October 2020.
62. Jonathan H Lin, Tetsuichiro Saito, David J Anderson, Cynthia Lance-Jones, Thomas M Jessell, and Silvia Arber. Functionally related motor neuron pool and muscle sensory afferent subtypes defined by coordinate ets gene expression. *Cell*, 95(3):393407, October 1998.
63. Jeremy S. Dasen, Bonnie C. Tice, Susan Brenner-Morton, and Thomas M. Jessell. A hox regulatory network establishes motor neuron pool identity and target-muscle connectivity. *Cell*, 123(3):477–491, nov 2005.
64. Jeremy S. Dasen, Alessandro De Camilli, Bin Wang, Philip W. Tucker, and Thomas M. Jessell. Hox repertoires for motor neuron diversity and connectivity gated by a single accessory factor, FoxP1. *Cell*, 134(2):304–316, jul 2008.
65. Olivia Hanley, Rediet Zewdu, Lisa J. Cohen, Heekyung Jung, Julie Lacombe, Polyxeni Philippidou, David H. Lee, Licia Selleri, and Jeremy S. Dasen. Parallel pbx -dependent pathways govern the coalescence and fate of motor columns. *Neuron*, 91(5):1005–1020, September 2016.
66. Polyxeni Philippidou and JeremyăS. Dasen. Hox genes: Choreographers in neural development, architects of circuit organization. *Neuron*, 80(1):1234, October 2013.
67. Mary C. Whitman and Elizabeth C. Engle. *Genetics of Strabismus*, page 68876905. Springer International Publishing, 2022.
68. Hans Supèr, Albert Martnez, José A. Del Ro, and Eduardo Soriano. Involvement of distinct pioneer neurons in the formation of layer-specific connections in the hippocampus. *The Journal of Neuroscience*, 18(12):46164626, June 1998.
69. Susan K. McConnell, Anirvan Ghosh, and Carla J. Shatz. Subplate neurons pioneer the first axon pathway from the cerebral cortex. *Science*, 245(4921):978982, September 1989.
70. David Bentley and Haig Keshishian. Pathfinding by peripheral pioneer neurons in grasshoppers. *Science*, 218(4577):10821088, December 1982.
71. C. M. BATE. Pioneer neurones in an insect embryo. *Nature*, 260(5546):5456, March 1976.
72. Susan H. Pike, Eloine F. Melancon, and Judith S. Eisen. Pathfinding by zebrafish motoneurons in the absence of normal pioneer axons. *Development*, 114(4):825831, April 1992.
73. Lynn Landmesser and Marcia G. Honig. Altered sensory projections in the chick hind limb following the early removal of motoneurons. *Developmental Biology*, 118(2):511531, December 1986.
74. Sheryl A. Scott. Skin sensory innervation patterns in embryonic chick hindlimbs deprived of motoneurons. *Developmental Biology*, 126(2):362374, April 1988.
75. Gavin J. Swanson and Julian Lewis. Sensory nerve routes in chick wing buds deprived of motor innervation. *Development*, 95(1):3752, June 1986.
76. Kathryn W. Tosney and Martha S. Hageman. Different subsets of axonal guidance cues are essential for sensory neurite outgrowth to cutaneous and muscle targets in the dorsal ramus of the embryonic chick. *Journal of Experimental Zoology*, 251(2):232244, August 1989.
77. Kathleen E. Whitlock and Monte Westerfield. A transient population of neurons pioneers the olfactory pathway in the zebrafish. *The Journal of Neuroscience*, 18(21):89198927, November 1998.
78. S. S. Easter Jr. and G. N. Nicola. The development of eye movements in the zebrafish (*Danio rerio*). *Developmental psychobiology*, 31(4):267–276, Dec 1997.
79. D. M. Noden, R. Marcucio, A. Borycki, and C. P. Emerson Jr. Differentiation of avian craniofacial muscles: I. patterns of early regulatory gene expression and myosin heavy chain synthesis. *Developmental Dynamics*, 216(2):96–112, Oct 1999.
80. R. A. McCrea, A. Strassman, and S. M. Highstein. Anatomical and physiological characteristics of vestibular neurons mediating the vertical vestibulo-ocular reflexes of the squirrel monkey. *The Journal of Comparative Neurology*, 264(4):571–594, October 1987.
81. Bruce Mendelson. Development of reticulospinal neurons of the zebrafish. ii. early axonal outgrowth and cell body position. *Journal of Comparative Neurology*, 251(2):172184, September 1986.
82. Kristen E. Severi, Ruben Portugues, João C. Marques, Donald M. O'Malley, Michael B. Orger, and Florian Engert. Neural control and modulation of swimming speed in the larval zebrafish. *Neuron*, 83(3):692–707, August 2014.
83. Tod R. Thiele, Joseph C. Donovan, and Herwig Baier. Descending control of swim posture by a midbrain nucleus in zebrafish. *Neuron*, 83(3):679–691, August 2014.
84. Wei-Chun Wang and David L. McLean. Selective responses to tonic descending commands by temporal summation in a spinal motor pool. *Neuron*, 83(3):708–721, aug 2014.
85. Masashi Tanimoto, Ikuko Watakabe, and Shin ichi Higashijima. Tiltable objective microscope visualizes discrimination of static and dynamic head movement originates at hair cells. *bioRxiv*, July 2022.
86. Eva M. Berg, Leander Mrowka, Maria Bertuzzi, David Madrid, Laurence D. Picton, and Abdeljabbar El Manira. Brainstem circuits encoding start, speed, and duration of swimming in adult zebrafish. *Neuron*, 111(3):372–386.e4, February 2023.
87. Masahito Yamagata, Joshua A. Weiner, and Joshua R. Sanes. Sidekicks. *Cell*, 110(5):649660, September 2002.
88. Masahito Yamagata and Joshua R. Sanes. Dscam and sidekick proteins direct lamina-specific synaptic connections in vertebrate retina. *Nature*, 451(7177):465469, January 2008.
89. Silvia Arber, David R Ladle, Jonathan H Lin, Eric Frank, and Thomas M Jessell. Ets gene er81 controls the formation of functional connections between group ia sensory afferents and motor neurons. *Cell*, 101(5):485498, May 2000.
90. Eline Pecho-Vrieseling, Markus Sigrist, Yutaka Yoshida, Thomas M. Jessell, and Silvia Arber. Specificity of sensory–motor connections encoded by sema3e–plxnd1 recognition. *Nature*, 459(7248):842–846, May 2009.
91. D. Bonanomi and S. L. Pfaff. Motor axon pathfinding. *Cold Spring Harbor Perspectives in Biology*, 2(3):a001735a001735, February 2010.
92. Xin Duan, Arjun Krishnaswamy, Irina DeălaăHuerta, and JoshuaăR. Sanes. Type ii cadherins guide assembly of a direction-selective retinal circuit. *Cell*, 158(4):793807, August 2014.
93. Timour Al-Khindi, Michael B. Sherman, Takashi Kodama, Preethi Gopal, Zhiwei Pan, James K. Kiraly, Hao Zhang, Loyal A. Goff, Sascha du Lac, and Alex L. Kolodkin. The transcription factor tbx5 regulates direction-selective retinal ganglion cell development and image stabilization. *Current Biology*, August 2022.

94. Yerbol Z Kurmangaliyev, Juyoun Yoo, Samuel A LoCascio, and S Lawrence Zipursky. Modular transcriptional programs separately define axon and dendrite connectivity. *eLife*, 8, November 2019.
95. Juyoun Yoo, Mark Dombrovski, Parmis Mirshahidi, Aljoscha Nern, Samuel A. LoCascio, S. Lawrence Zipursky, and Yerbol Z. Kurmangaliyev. Brain wiring determinants uncovered by integrating connectomes and transcriptomes. *Current Biology*, 33(18):3998–4005.e6, September 2023.
96. Jeremy S. Dasen. *Chapter 4 Transcriptional Networks in the Early Development of SensoryMotor Circuits*, page 119148. Elsevier, 2009.
97. Nikhil Sharma, Kali Flaherty, Karina Lezgiyeva, Daniel E. Wagner, Allon M. Klein, and David D. Ginty. The emergence of transcriptional identity in somatosensory neurons. *Nature*, 577(7790):392398, January 2020.
98. Brikha R. Shrestha, Chester Chia, Lorna Wu, Sharon G. Kujawa, M. Charles Liberman, and Lisa V. Goodrich. Sensory neuron diversity in the inner ear is shaped by activity. *Cell*, 174(5):1229–1246.e17, August 2018.
99. William A. Alaynick, Thomas M. Jessell, and Samuel L. Pfaff. Snapshot: Spinal cord development. *Cell*, 146(1):178–178.e1, July 2011.
100. Marc Tessier-Lavigne and Corey S. Goodman. The molecular biology of axon guidance. *Science*, 274(5290):11231133, November 1996.
101. Corey S. Goodman and Carla J. Shatz. Developmental mechanisms that generate precise patterns of neuronal connectivity. *Cell*, 72:7798, January 1993.
102. Olivia Spead, Trevor Moreland, Cory J. Weaver, Irene Dalla Costa, Brianna Hegarty, Kenneth L. Kramer, and Fabienne E. Poulain. Teneurin trans-axonal signaling prunes topographically missorted axons. *Cell Reports*, 42(3):112192, March 2023.
103. A. Zecca, S. Dyballa, A. Voltes, R. Bradley, and C. Pujades. The order and place of neuronal differentiation establish the topography of sensory projections and the entry points within the hindbrain. *Journal of Neuroscience*, 35(19):7475–7486, may 2015.
104. Sylvia Dyballa, Thierry Savy, Philipp Germann, Karol Mikula, Mariana Remesikova, Róbert Špir, Andrea Zecca, Nadine Peyriéras, and Cristina Pujades. Distribution of neurosensory progenitor pools during inner ear morphogenesis unveiled by cell lineage reconstruction. *eLife*, 6, jan 2017.
105. B. Fritzsch and D.H. Nichols. Dii reveals a prenatal arrival of efferents at the differentiating otocyst of mice. *Hearing Research*, 65(12):5160, February 1993.
106. Joseph Altman and Shirley A. Bayer. *Development of the Cranial Nerve Ganglia and Related Nuclei in the Rat*. Springer Berlin Heidelberg, 1982.
107. Jo Ann McConnell and John W. Sechrist. Identification of early neurons in the brainstem and spinal cord: I. an autoradiographic study in the chick. *Journal of Comparative Neurology*, 192(4):769783, August 1980.
108. Adel Maklad and Bernd Fritzsch. Development of vestibular afferent projections into the hindbrain and their central targets. *Brain Research Bulletin*, 60(56):497510, June 2003.
109. Franois Auclair, Raymond Marchand, and Joel C. Glover. Regional patterning of reticulospinal and vestibulospinal neurons in the hindbrain of mouse and rat embryos. *The Journal of Comparative Neurology*, 411(2):288300, August 1999.
110. Joseph Altman and Shirley A. Bayer. Development of the brain stem in the rat. V. Thymidine-radiographic study of the time of origin of neurons in the midbrain tegmentum. *The Journal of Comparative Neurology*, 198(4):677–716, Jun 1981.
111. Marjorie D. Shaw and Keith E. Alley. Generation of the ocular motor nuclei and their cell types in the rabbit. *The Journal of Comparative Neurology*, 200(1):69–82, Jul 1981.
112. Luis Puelles and Alain Privat. Do oculomotor neuroblasts migrate across the midline in the fetal rat brain? *Anatomy and Embryology*, 150(2):187206, 1977.
113. Cecilia B. Moens and Victoria E. Prince. Constructing the hindbrain: Insights from the zebrafish. *Developmental Dynamics*, 224(1):1–17, April 2002.
114. Amina Kinkhabwala, Michael Riley, Minoru Koyama, Joost Monen, Chie Satou, Yukiko Kimura, Shin ichi Higashijima, and Joseph Fetcho. A structural and functional ground plan for neurons in the hindbrain of zebrafish. *Proceedings of the National Academy of Sciences*, 108(3):1164–1169, January 2011.
115. Dylan R. Farnsworth, Lauren M. Saunders, and Adam C. Miller. A single-cell transcriptome atlas for zebrafish development. *Developmental Biology*, 459(2):100–108, March 2020.
116. Monica Tambalo, Richard Mitter, and David G. Wilkinson. A single cell transcriptome atlas of the developing zebrafish hindbrain. *Development*, January 2020.
117. Juan E. Ferrario, Pranetha Baskaran, Christopher Clark, Aenea Hendry, Oleg Lerner, Mark Hintze, James Allen, John K. Chilton, and Sarah Guthrie. Axon guidance in the developing ocular motor system and duane retraction syndrome depends on semaphorin signaling via alpha2-chimaerin. *Proceedings of the National Academy of Sciences*, 109(36):1466914674, August 2012.
118. Sarah Guthrie. Patterning and axon guidance of cranial motor neurons. *Nature Reviews Neuroscience*, 8(11):859871, November 2007.
119. Kenna D. Peusner and D.K. Morest. The neuronal architecture and topography of the nucleus vestibularis tangentialis in the late chick embryo. *Neuroscience*, 2(2):189–IN2, April 1977.
120. April E. Ronca, Alison J. French, and Jeffrey D. Smith. Translating basic research to astronaut health in space: Nasa ames rodent specimen biobanking for the human research program. *Gravitational and Space Research*, 4(2):7074, December 2016.
121. Bruce B. Riley and Stephen J. Moorman. Development of utricular otoliths, but not saccular otoliths, is necessary for vestibular function and survival in zebrafish. *Journal of Neurobiology*, 43(4):329–337, 2000.
122. Richard Roberts, Jeffrey Elsner, and Martha W. Bagnall. Delayed otolith development does not impair vestibular circuit formation in zebrafish. *Journal of the Association for Research in Otolaryngology*, 18(3):415–425, March 2017.
123. Florian Ulrich, Charlotte Grove, Jesús Torres-Vázquez, and Robert Baker. Development of functional hindbrain oculomotor circuitry independent of both vascularization and neuronal activity in larval zebrafish. *Current Neurobiology*, 7:62–73, 2014.
124. Johannes Schindelin, Ignacio Arganda-Carreras, Erwin Frise, Verena Kaynig, Mark Longair, Tobias Pietzsch, Stephan Preibisch, Curtis Rueden, Stephan Saalfeld, Benjamin Schmid, Jean-Yves Tinevez, Daniel James White, Volker Hartenstein, Kevin Eliceiri, Pavel Tomancak, and Albert Cardona. Fiji: an open-source platform for biological-image analysis. *Nature Methods*, 9(7):676–682, Jun 2012.
125. S. J. C. Caron, D. Prober, M. Choy, and A. F. Schier. *In vivo* birthdating by BAPTISM reveals that trigeminal sensory neuron diversity depends on early neurogenesis. *Development*, 135(19):3259–3269, Aug 2008.
126. Gabrielle R. Barsh, Adam J. Isabella, and Cecilia B. Moens. Vagus motor neuron topographic map determined by parallel mechanisms of hox5 expression and time of axon initiation. *Current Biology*, 27(24):3812–3825.e3, December 2017.
127. Rodrigo Ibarra-García-Padilla, Aubrey Gaylon Adam Howard, Eileen Willey Singleton, and Rosa Anna Uribe. A protocol for whole-mount immuno-coupled hybridization chain reaction (wichcr) in zebrafish embryos and larvae. *STAR Protocols*, 2(3):100709, September 2021.
128. Emily Kuehn, David S. Clausen, Ryan W. Null, Bria M. Metzger, Amy D. Willis, and B. Duygu Özpolat. Segment number threshold determines juvenile onset of germline cluster expansion in platynereis dumerilii. *Journal of Experimental Zoology Part B: Molecular and Developmental Evolution*, 338(4):225240, November 2021.
129. Michael I Love, Wolfgang Huber, and Simon Anders. Moderated estimation of fold change and dispersion for rna-seq data with deseq2. *Genome Biology*, 15(12), December 2014.
130. Samuel L. Pfaff, Monica Mendelsohn, Colin L. Stewart, Thomas Edlund, and Thomas M. Jessell. Requirement for lim homeobox gene isl1 in motor neuron generation reveals a motor neuron dependent step in interneuron differentiation. *Cell*, 84(2):309320, January 1996.
131. Mika Tokumoto, Zhiyuan Gong, Tatsuya Tsubokawa, Choy L. Hew, Keiichi Uyemura, Yoshiki Hotta, and Hitoshi Okamoto. Molecular heterogeneity among primary motoneurons and within myotomes revealed by the differential mrna expression of novel islet-1 homologs in embryonic zebrafish. *Developmental Biology*, 171(2):578589, October 1995.
132. Victoria E. Prince, Cecilia B. Moens, Charles B. Kimmel, and Robert K. Ho. Zebrafish hox genes: expression in the hindbrain region of wild-type and mutants of the segmentation gene, valentino. *Development*, 125(3):393406, February 1998.
133. Yuhan Hao, Stephanie Hao, Erica Andersen-Nissen, William M. Mauck, Shiwei Zheng, Andrew Butler, Maddie J. Lee, Aaron J. Wilk, Charlotte Darby, Michael Zager, Paul Hoffman, Marlon Stoeckius, Efthymia Papalexi, Eleni P. Mimitou, Jaison Jain, Avi Srivastava, Tim Stuart, Lamar M. Fleming, Bertrand Yeung, Angela J. Rogers, Juliana M. McElrath, Catherine A. Blish, Raphael Gottardo, Peter Smibert, and Rahul Satija. Integrated analysis of multimodal single-cell data. *Cell*, 184(13):3573–3587.e29, June 2021.
134. B. Efron and R. Tibshirani. Bootstrap methods for standard errors, confidence intervals, and other measures of statistical accuracy. *Statistical Science*, 1(1):54–75, February 1986.

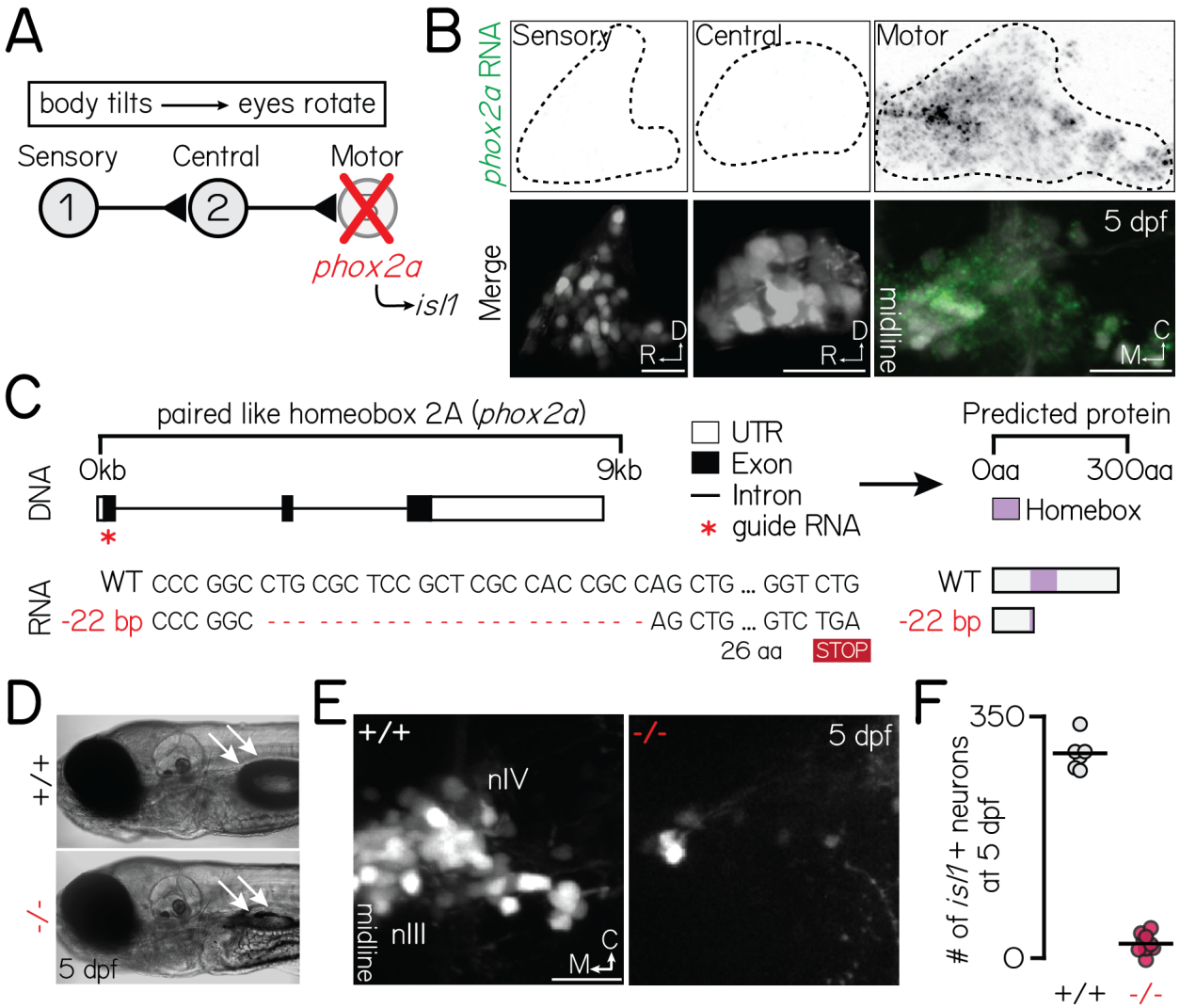


**Figure 1: *phox2a* loss-of-function mutants fail to develop nIII/nIV motor neurons and vertical eye rotation behavior.**
Associated with Figure S2.
**(A)** Schematic of vestibulo-ocular reflex circuitry and the genetic loss-of-function approach used to perturb motor-derived signals.
**(B)** Fluorescent *in situ* hybridization showing *phox2a* transcript expression in statoacoustic ganglion sensory afferents (left), central projection neurons in the tangential nucleus (middle), or nIII/nIV extraocular motor neurons (right) at 5 days post-fertilization (dpf). Top: probe only, nuclei outlined with dashed lines. Bottom: probe (green) merged with somata, labeled by *Tg(-6.7Tru.Hcrtr2:GAL4-VP16);Tg(UAS-E1b:Kaede)* (sensory, central) or *Tg(isl1:GFP)* (motor).
**(C)** Schematic of CRISPR/Cas9 mutagenesis approach. Top: Red star shows location of guides against *phox2a* DNA. Bottom: RNA sequence in wildtype and *phox2a*$^{d22}$ alleles. Red dashed lines show deleted sequence; "STOP" box shows predicted premature stop codon due to deletion. Right shows predicted protein sequence.
**(D)** Transmitted light image of a 5 dpf wildtype (top) and *phox2a* null mutant (bottom). White arrows point to a normally inflated (top) or absent (bottom) swim bladder.
**(E)** Images of nIII/nIV motor neurons in one hemisphere, labeled by *Tg(isl1:GFP)*, in wildtype siblings (left) and *phox2a* null mutants (right) at 5 dpf. Scale bar, 20 μm.
**(F)** Quantification of the number of *Tg(isl1:GFP)*+ neurons in nIII/nIV from N=6 wildtype siblings and N=10 *phox2a* null mutants.

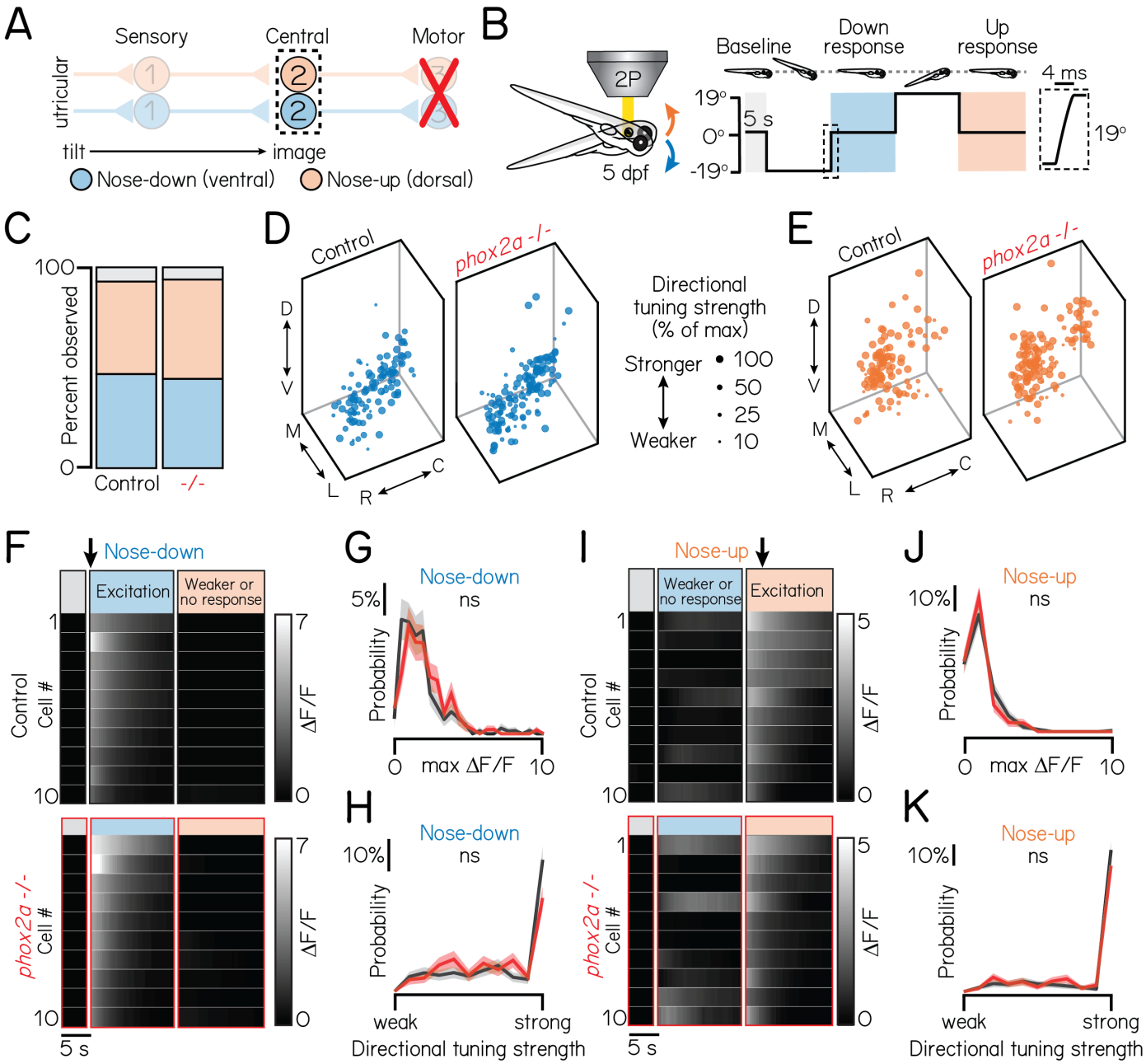


**Figure 2: Motor neurons are dispensable for proper connectivity between utricular sensory afferents and projection neurons.**
Associated with Table 1.
**(A)** Schematic of pitch vestibulo-ocular reflex circuitry. Dashed lines outline projection neurons as calcium imaging target. Nose-down/eyes-up channel represented with blue; orange, nose-up/eyes-down.
**(B)** Schematic of tonic pitch-tilt stimulus delivered with Tilt-In-Place Microscopy (TIPM). Shaded regions show calcium imaging windows when fish were oriented horizontally immediately following tilts. Inset shows timecourse of the rapid step to restore horizontal position after tilts. Imaging experiments used larvae from the *Tg(isl1:GFP);Tg(-6.7Tru.Hcrtr2:GAL4-VP16);Tg(UAS:GCaMP6s)* line.
**(C)** Proportion of subtypes observed in sibling controls and *phox2a* null mutants. Blue: nose-down. Orange: nose-up. Grey: Neurons without directional tuning (criteria in Methods).
**(D/E)** Soma position of nose-down (blue) and nose-up (orange) neurons in sibling controls (left) and *phox2a* null mutants (right). Soma size scaled by strength of directional selectivity (min=0; max=1; see Methods).
**(F/I)** Heatmaps showing example tilt responses from nose-down (F) or nose-up (I) neurons in sibling controls (top) and *phox2a* null mutants (bottom). n=10 neurons with strongest ΔF/F responses to tilts shown. Each row shows an individual neuron. Shaded bars show calcium imaging window immediately following restoration from eccentric position. Black arrow points to first second of tilt response used for analyses.
**(G/J)** Distributions of maximum ΔF/F responses to tilts for nose-down (G) or nose-up (J) neurons in sibling controls (black) and *phox2a* null mutants (red). Solid and shaded lines show mean and standard deviation, respectively, of bootstrapped data (Methods)
**(H/K)** Distributions of directional tuning score to tilts for nose-down (H) or nose-up (K) neurons in sibling controls (black) and *phox2a* null mutants (red). Tuning score ranges from 0 (equal responses to both tilt directions, no tuning) to 1 (responses to one tilt direction only); criteria detailed in Methods. Solid and shaded lines show mean and standard deviation, respectively, of bootstrapped data.

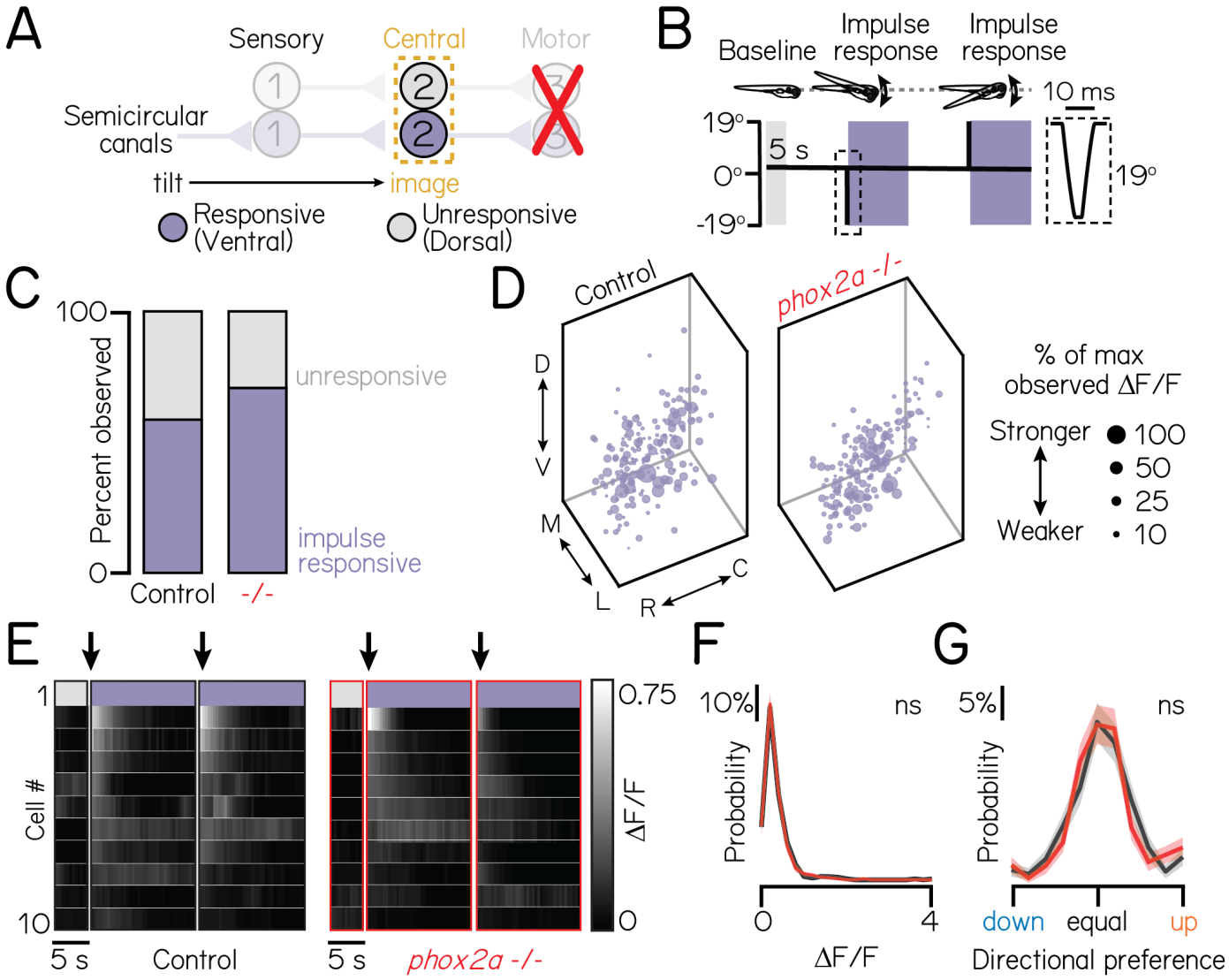


**Figure 3: Motor neurons are dispensable for proper connectivity between semicircular canal sensory afferents and projection neurons.** Associated with Table 1.

**(A)** Schematic of impulse tilt experiments. Yellow dashed lines outline projection neurons as calcium imaging target. Impulse-responsive neurons (ventrally-localized) shown with purple; unresponsive neurons, grey.

**(B)** Schematic of impulse stimuli delivered with TIPM. Shaded regions show calcium imaging windows at horizontal immediately following impulses. Inset shows timecourse of impulse stimulus. Imaging experiments used larvae from the *Tg(isl1:GFP);Tg(-6.7Tru.Hcrtr2:GAL4-VP16);Tg(UAS:GCaMP6s)* line.

**(C)** Proportion of impulse-responsive (purple) and unresponsive (grey) neurons observed in sibling controls and *phox2a* null mutants.

**(D)** Soma position of impulse-responsive neurons in sibling controls (left) and *phox2a* null mutants (right). Soma size scaled by strength of calcium response (ΔF/F), normalized by max observed ΔF/F.

**(E)** Heatmaps showing example impulse responses from neurons in sibling controls (left) and *phox2a* null mutants (right). n=10 example neurons shown. Each row shows an individual neuron. Shaded bars show calcium imaging window immediately following impulse delivery. Black arrow points to first second of tilt response used for analyses. Note smaller scale (0-0.75) of impulse responses relative to Figures 2F and 2I.

**(F)** Distributions of maximum ΔF/F responses to impulses in sibling controls (black) and *phox2a* null mutants (red). Solid and shaded lines show mean and standard deviation, respectively, from bootstrapped data.

**(G)** Distributions of directional tuning score to impulses in sibling controls (black) and *phox2a* null mutants (red). Tuning score ranges from 0 (equal responses to both tilt directions, no tuning) to 1 (responses to one tilt direction only); criteria detailed in Methods. Solid and shaded lines show mean and standard deviation, respectively, from bootstrapped data.

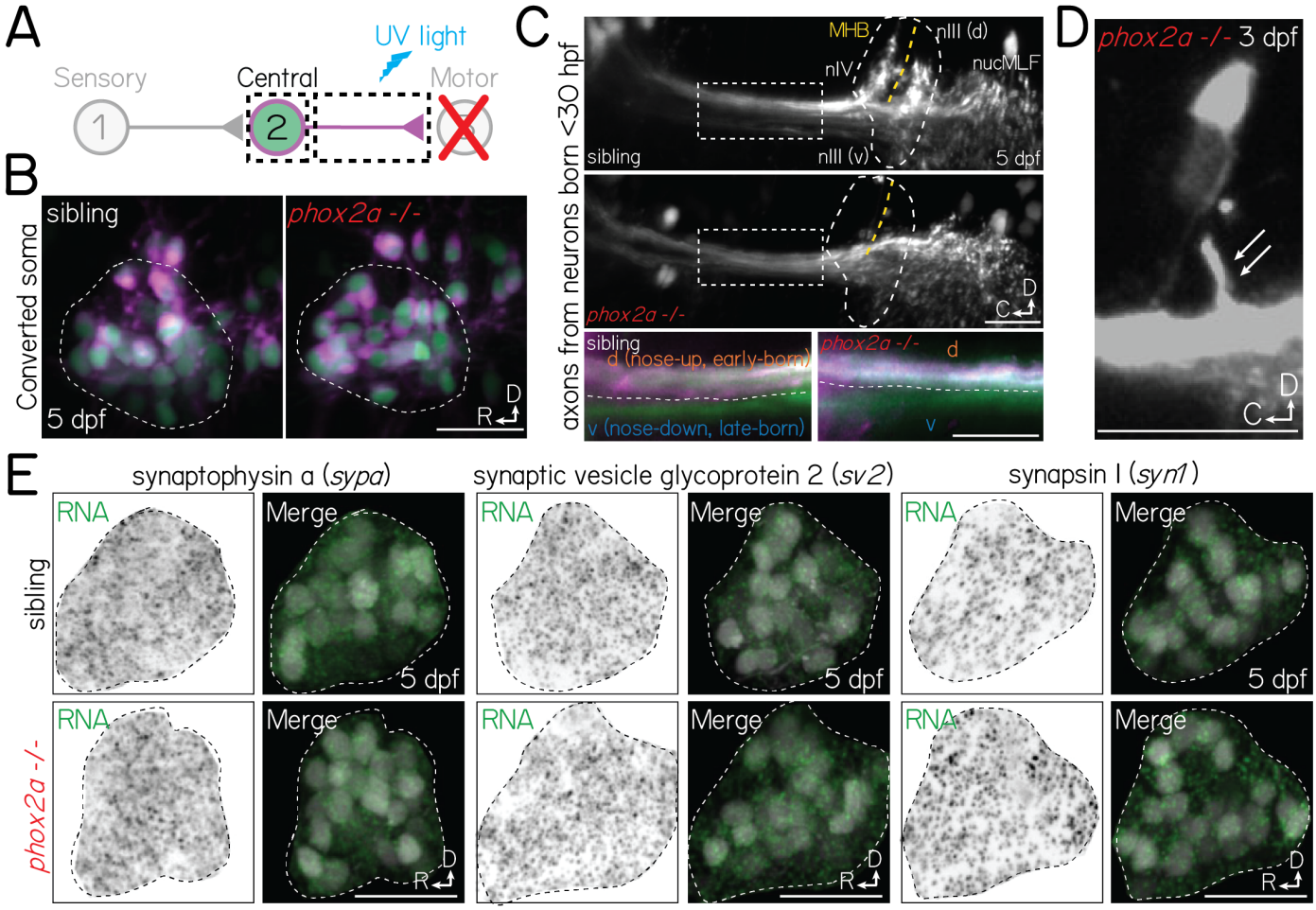


**Figure 4: Projection neurons are anatomically and molecularly poised to assemble with motor neuron partners in *phox2a* mutants.**
**(A)** Schematic of retrograde photofill experiments. Projection neuron axons expressing the photolabile protein Kaede are targeted at the midbrain-hindbrain boundary with ultraviolet light. Converted protein (magenta) retrogradely diffuses to the soma, while the unconverted nucleus remains green.
**(B)** Projection neuron somata in sibling controls (left) and *phox2a* null mutants (right) after retrograde photolabeling. Experiments performed at 5 dpf. Neurons visualized in *Tg(isl1:GFP);Tg(-6.7Tru.Hcrtr2:GAL4-VP16);Tg(UAS:E1b-Kaede).*
**(C)** Top two panels: Projection neuron axons at the hindbrain (inset) and midbrain-hindbrain boundary in sibling controls (top) and *phox2a* null mutants (bottom). Axons visualized using *Tg(isl1:GFP);Tg(-6.7Tru.Hcrtr2:GAL4-VP16);Tg(UAS:E1b-Kaede).* White dashed outline (circle) shows arborization fields in nIII/nIV. Dashed box over axons shows location of two bottom panels. MHB and yellow dashed line, midbrain-hindbrain boundary. nucMLF: nucleus of the longitudinal fasciculus. Bottom two panels: Zoom of axons (dashed rectangle above). Spatial segregation between early-born (magenta+green) and late-born (green only) axons. White dashed line reflects separation between dorsal (nose-up, early-born) and ventral (nose-down, late-born) axon bundles. Image at 5 dpf in sagittal view.
**(D)** Projection neuron axon bundle in a *phox2a* null mutant at 3 dpf. White arrows point to single collateral to two nIII/nIV neurons that were not eliminated following *phox2a* knockout.
**(E)** Fluorescent *in situ* hybridization against RNA for three pre-synaptic markers: synaptophysin a (*sypa*; left), synaptic vesicle glycoprotein 2 (*sv2*, middle), and synapsin I (*syn1*, right). Top row, sibling controls. Bottom row, *phox2a* null mutants. For each panel set, left images show *in situ* probe expression (green) and right images show merge with projection neurons labeled in *Tg(-6.7Tru.Hcrtr2:GAL4-VP16);Tg(UAS:E1b-Kaede).* Dashed lines outline the projection nucleus. Cell and transcript expression outside the projection nucleus is removed for visual clarity. Images taken at 5 dpf in sagittal mount. All scale bars, 20 μm.

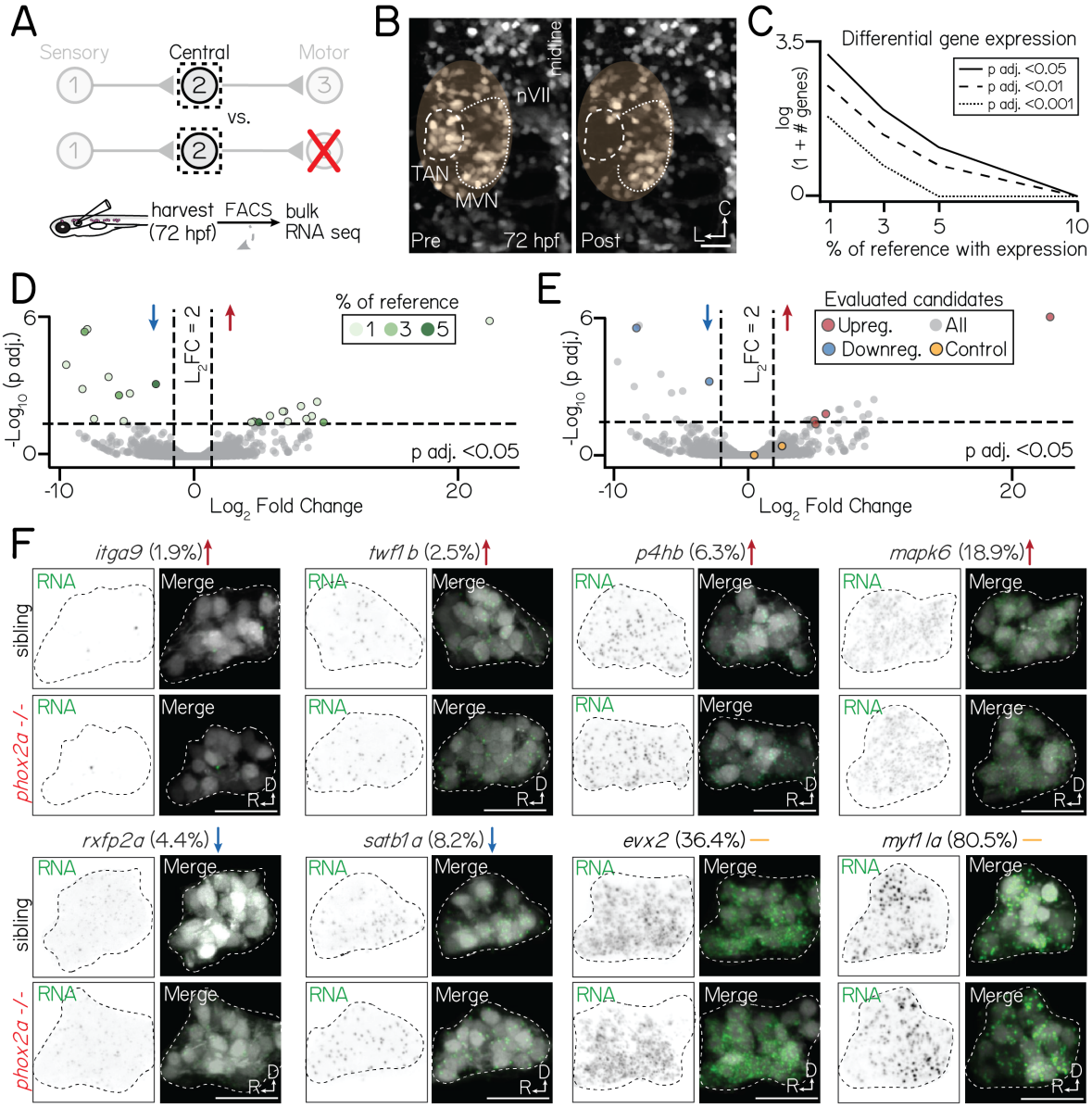


**Figure 5: Motor neurons are dispensable for normal transcriptional profiles of projection neurons.**
Associated with Figure S3-Figure S6, Table 3.

**(A)** Schematic of sequencing approach. Central projection neurons (*Tg(-6.7Tru.Hcrtr2:GAL4-VP16);Tg(UAS:E1b-Kaede)*) are harvested from 3 dpf larvae. Flow cytometry is used to exclude neurons not labelled by *Tg(-6.7Tru.Hcrtr2:GAL4-VP16)*. Bulk RNA sequencing is performed to compare the profiles of projection neurons in siblings and *phox2a* null mutants.

**(B)** Example of projection neurons before (left) and after (right) harvesting. Neurons visualized with *Tg(isl1:GFP);Tg(-6.7Tru.Hcrtr2:GAL4-VP16);Tg(UAS:E1b-Kaede)*. Dashed lines outline projection neurons in the tangential nucleus; dotted lines, medial vestibular nucleus. Yellow region shows margin of harvesting error: non-projection neurons that may be included in bulk sequencing dataset.

**(C)** Number of differentially expressed genes in projection neurons at 3 dpf after applying progressive filters based on gene expression in a reference single-cell dataset. Data shown on logarithmic scale. Solid, dashed, and dotted lines represent differentially-expressed gene with p adjusted<0.5, p adjusted<0.01, or p adjusted<0.001 significance, respectively.

**(D)** Volcano plot showing differentially expressed genes in projection neurons between control and *phox2a* null larvae at 3 dpf. Dashed lines represent significance cutoffs: horizontal line, p adjusted>0.05; vertical line, $Log_2$ Fold Change > 2.0. Each circle is a gene. Genes to the left and right of 0 on the horizontal axis show downregulated and upregulated genes, respectively. Colors indicate percent of reference cells that express a given gene. Grey-colored genes are below both significance thresholds.

**(E)** Same data as Figure 5D. Colored genes show eight candidates evaluated with fluorescent *in situ* hybridization: red, upregulated; blue, downregulated; yellow, highly-expressed controls (*evx2*.

**(F)** Fluorescent *in situ* hybridization against candidate genes that met projection neuron filter criteria. Top row shows sibling controls; bottom row, *phox2a* null mutants. For each gene, left panels show RNA probe (green) and right panels show merge with projection neurons labeled by *Tg(-6.7Tru.Hcrtr2:GAL4-VP16)* (grey). Dashed lines outline the projection nucleus. Cell and transcript expression outside the projection nucleus is masked for visual clarity. Arrows denote whether genes are upregulated (red), downregulated (blue), or not significantly changed (yellow). Percentage refers to fraction of cells in a single-cell RNA sequencing reference atlas (Methods) with detected transcript. Candidates: *itga9* ($log_2$ fold change=23.0, p adj.=$3.9x10^{-6}$), *twf1b* ($log_2$ fold change=5.9, p adj.=0.024, *p4hb* ($log_2$ fold change=5.1, p adj.=0.04), *mapk6* ($log_2$ fold change=5.1, p adj.=0.06), *rxfp2a* ($log_2$ fold change=-8.5, p adj.=$1.1x10^{-5}$), *satb1a* (($log_2$ fold change=-3.0, p adj.=0.001), *evx2* ($log_2$ fold change=0.46, p adj.=0.99), *myt1la* (($log_2$ fold change=2.6, p adj.=0.44) . All scale bars, 20 μm.

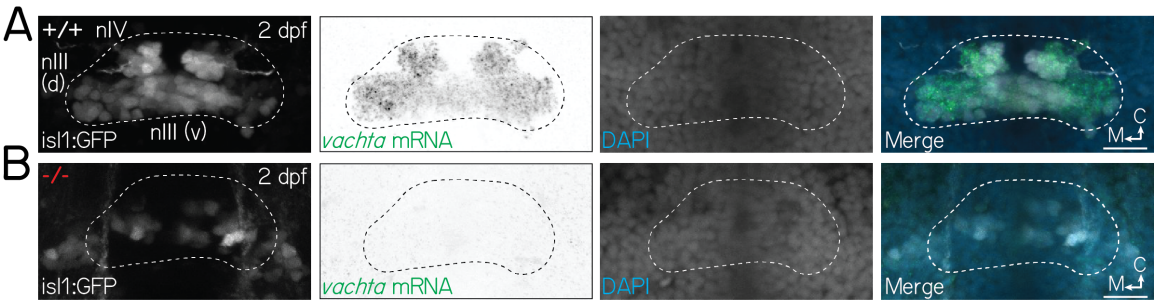


**Figure S1: Extraocular motor neuron fate is perturbed in *phox2a* mutants**
Associated with Figure 1.
**(A)** Fluorescent *in situ* hybridization images of nIII/nIV motor neurons, labeled by *Tg(isl1:GFP)*, in wildtype larvae at 2 dpf. Panels from left to right show: (1) *isl1+* motor neurons, (2) mRNA for *vachta*, a marker for cholinergic motor neurons, (3) DAPI, and (4) merge. White dashed lines show the extent of nIII/nIV.
**(B)** Loss of both *isl1* and *vachta* identity in nIII/nIV motor neurons in *phox2a* mutants at 2 dpf. All scale bars, 20 μm.

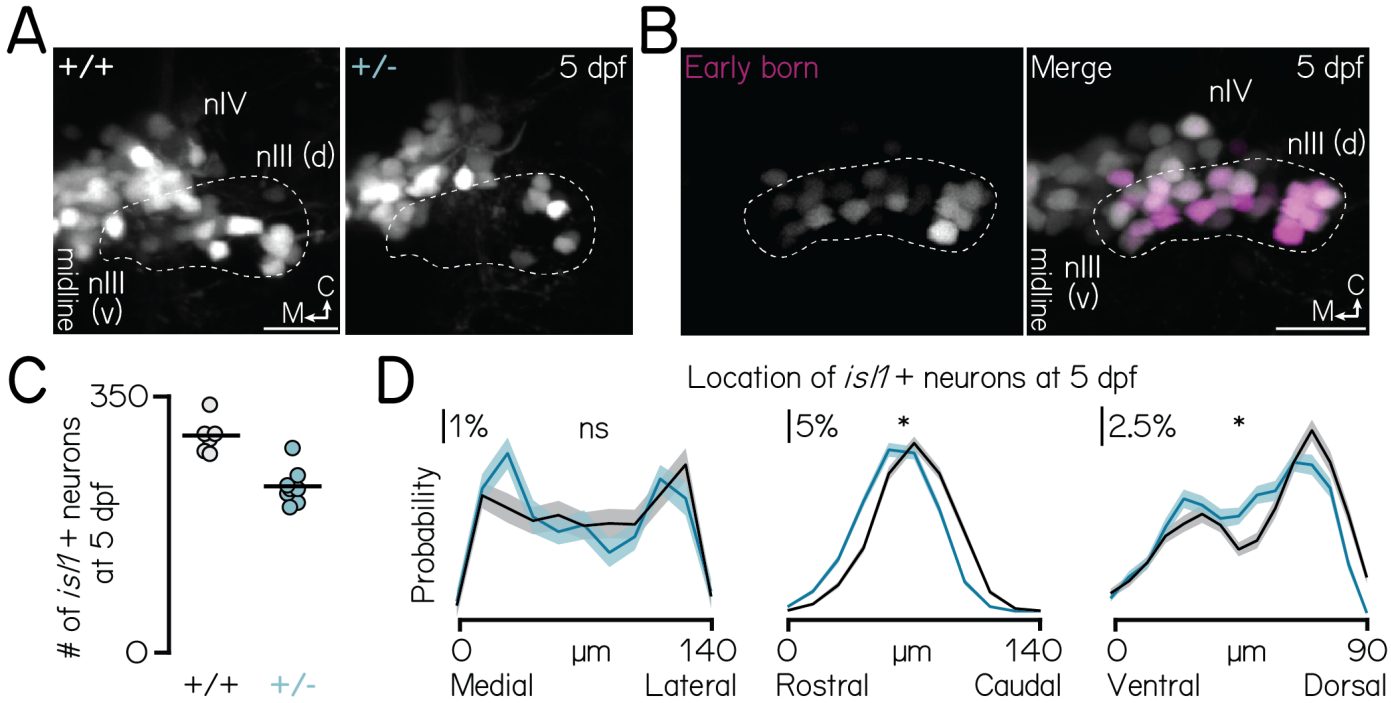


**Figure S2: *phox2a* specifies nIII motor neuron fate in a dose- and birthdate-dependent manner.**
Associated with Figure 1.
**(A)** Images of nIII/nIV motor neurons, labeled in *Tg(isl1:GFP)*, in wildtype siblings (left) and *phox2a* heterozygotes (middle) at 5 dpf. Wildtype image same as in Figure 1E. One hemisphere shown. White dashed lines outline the dorsal extent of nIII, which contains inferior rectus and medial rectus neurons[33]. Scale bar, 20 μm.
**(B)** Location of the earliest-born neurons in nIII/nIV (left, magenta) against all nIII/nIV neurons labeled in *Tg(isl1:Kaede)* (right, grey). Larvae birthdated at 34 hpf (Methods). One hemisphere shown. White dashed lines outline the dorsal extent of nIII. Scale bar, 20 μm.
**(C)** Quantification of the number of *Tg(isl1:GFP)*+ neurons in nIII/nIV from N=6 wildtype siblings (grey) and N=8 *phox2a* heterozygotes (teal). Wildtype data same as Figure 1F.
**(D)** Distributions showing probability of nIII/nIV soma location across each spatial axis in wildtype (black) and heterozygous (teal) *phox2a* larvae. Solid and shaded lines show mean and standard deviation, respectively, from bootstrapped data. Data from same fish quantified in Figure S2C. ns, not significant; star, significant at the $p<0.001$ level.

A

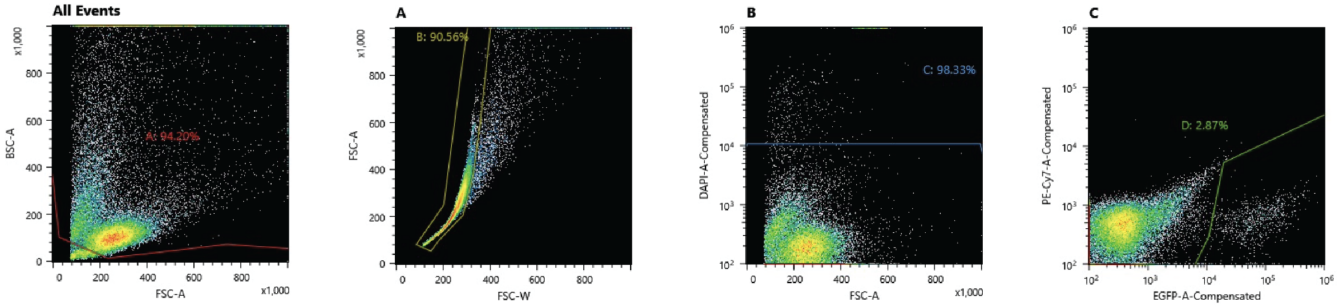


**Figure S3: Flow cytometry gating strategy to sort fluorescently-labeled neurons for bulk RNA sequencing.**
Associated with Figure 5.
**(A)** Sequential gates used to sort fluorescent neurons labeled with *Tg(-6.7Tru.Hcrtr2:GAL4-VP16);Tg(UAS-E1b:Kaede);Tg(isl1:GFP)*. Gate A excluded presumptive debris (small cells). Gate B isolated single cells and excluded large cells and doublets. Gate C excluded DAPI+ (dead or unhealthy) neurons. Gate D isolated fluorescent (GFP or Kaede+) neurons; neurons in this gate were sorted. Gates were set using negative controls (not shown; Methods). Gates shown for one of four experimental repeats.

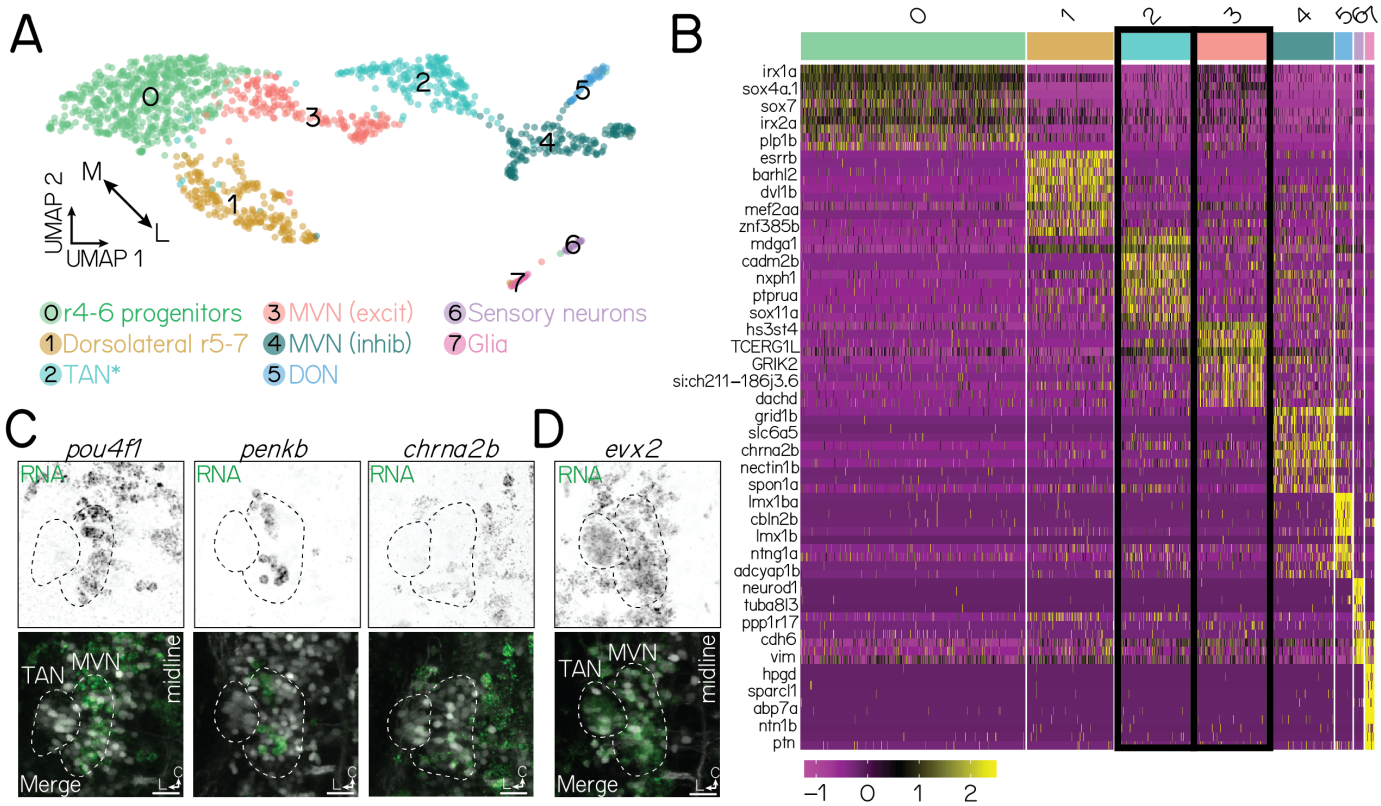


**Figure S4: Molecular identification of projection neurons using a reference single-cell RNA sequencing atlas.**
Associated with Figure 5.
**(A)** UMAP visualization of a single-cell RNA sequencing atlas of n=1,468 neurons labeled in *Tg(-6.7Tru.Hcrtr2:GAL4-VP16);Tg(UAS-E1b:Kaede)*, generated with 10x Genomics (Methods). Each circle is a single neuron. Neurons are clustered (colors) according to their transcriptional identity. Annotations are based on validated marker genes (data not shown). TAN, tangential nucleus; MVN, medial vestibular nucleus; r, rhombomere; DON, dorsal octavolateral nucleus. Note: Cluster 2 is broadly inclusive of lateral, excitatory vestibular projection neurons near the ventral base of the otic capsule. It includes, but is not exclusive to, the tangential nucleus.
**(B)** Heatmap showing genes unique to each annotated cluster. Each row is a gene; names unlisted for clarity. Columns show distinct clusters. Color bar on top reflects clusters in Figure S4A. Yellow and purple reflect stronger or weaker gene expression, respectively. Black outlines show two populations of interest: tangential nucleus neurons and medial vestibular nucleus neurons.
**(C)** Fluorescent *in situ* hybridization against three markers (*pou4f1*, *penkb*, *chrna2b*) that are negative for tangential nucleus projection neurons and positive for medial vestibular nucleus neurons. Top row shows RNA expression (green); bottom row, merge with neurons labeled in *Tg(-6.7Tru.Hcrtr2:GAL4-VP16);Tg(UAS-E1b:Kaede)*. Dashed lines outline the tangential nucleus (TAN) and medial vestibular nucleus (MVN). Data from 72 hpf larvae. Images shown in an axial view.
**(D)** Fluorescent *in situ* hybridization against a positive marker (*evx2*) for both tangential nucleus and medial vestibular nucleus neurons. All scale bars, 20 µm.

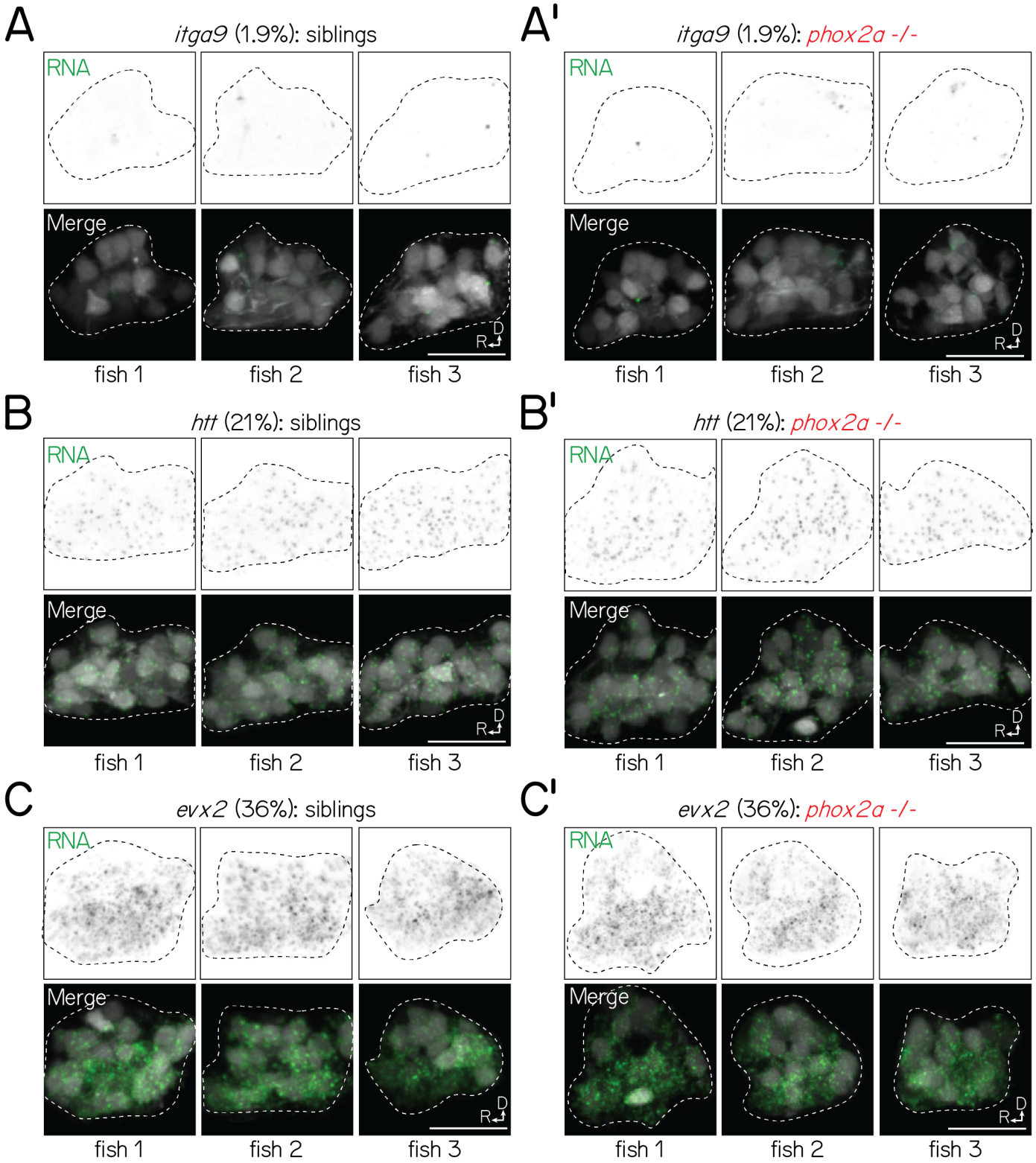


**Figure S5: Visualization of transcripts in siblings and *phox2a* null mutants with fluorescent *in situ* hybridization is (1) consistent across larvae and (2) scales with predicted detection in projection neurons.**
Associated with Figure 5.
**(A-A')** Fluorescent *in situ* hybridization against *itga9* for three sibling (A) or *phox2a* null mutant (A') larvae (72 hpf), imaged with identical conditions. Left column shows RNA (green); right column, merge with projection neurons visualized with *Tg(-6.7Tru.Hcrtr2:GAL4-VP16);Tg(UAS-E1b:Kaede)* (grey). Dashed lines outline the projection nucleus. Cell and transcript expression outside the projection nucleus is removed for visual clarity. Percentage (1.9%) refers to fraction of cells in a single-cell RNA sequencing reference atlas (Methods) with detected transcript. All scale bars, 20 µm.
**(B-B')** Fluorescent *in situ* hybridization against *htt* for three sibling (B) and *phox2a* mutant (B') larvae (72 hpf).
**(C-C')** Fluorescent *in situ* hybridization against *evx2* for three sibling (C) and *phox2a* mutant (C') larvae (72 hpf).

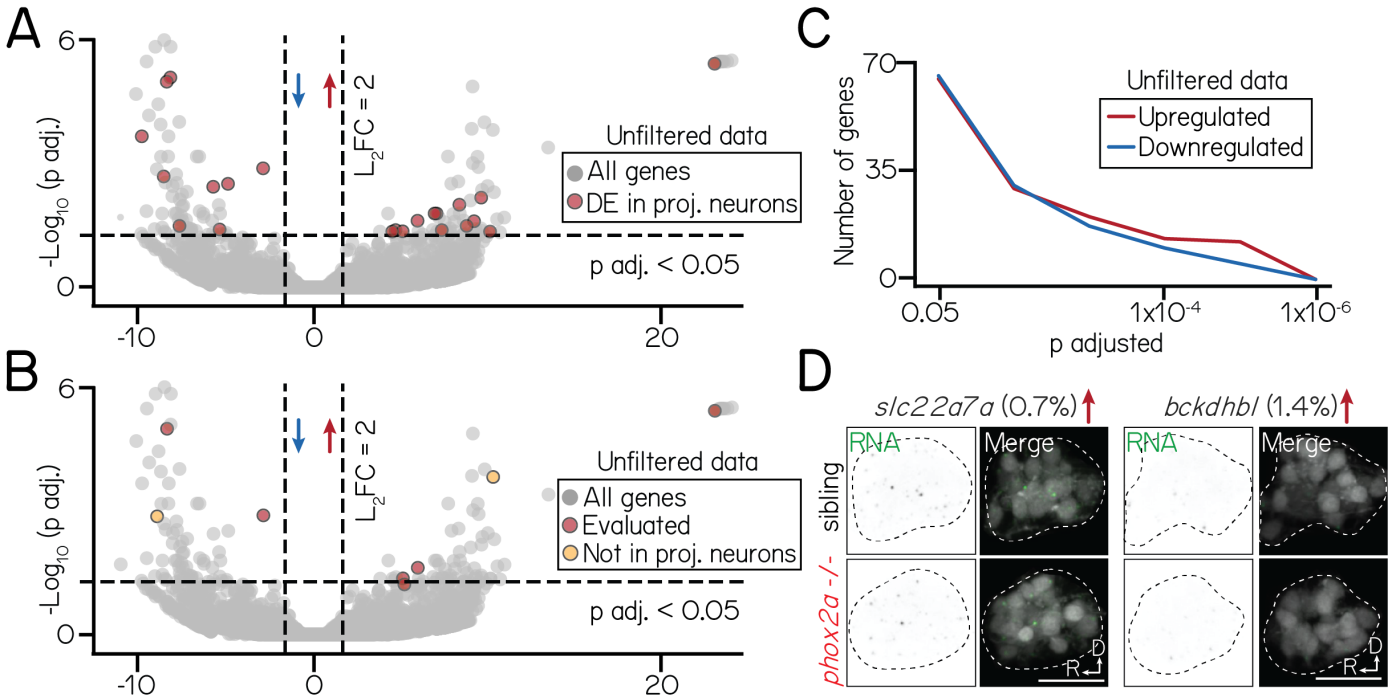


**Figure S6: Differential gene expression in an unfiltered bulk sequencing dataset of siblings and *phox2a* mutants.**
Associated with Figure 5.
**(A)** Volcano plot showing differentially expressed genes across an unfiltered bulk RNA sequencing dataset. Dashed lines represent significance cutoffs: horizontal line, p adjusted>0.05; vertical line, $Log_2$ Fold Change > 2.0. Each circle is a gene. Genes to the left and right of 0 on the horizontal axis show downregulated and upregulated genes, respectively. Red color shows genes that are differentially expressed in a filtered subset of projection neurons (Figure 5). Grey-colored genes are below both significance thresholds.
**(B)** Same data as Figure S6A, now highlighting candidate genes evaluated by fluorescent *in situ* (Figure 5) with red. Two candidates (yellow) that did not meet projection neuron filter criteria (Methods) are shown in Figure S6D; remaining candidates (included in filtered data) shown in Figure 5F.
**(C)** Same data as Figure S6A-Figure S6B, showing the number of differentially expressed genes at progressive significance thresholds (p adjusted). Red and blue lines show the number of significantly upregulated and downregulated genes, respectively.
**(D)** Fluorescent *in situ* hybridization against two differentially expressed genes, *slc22a7a* ($log_2$ fold change=10.2, p adj.=$1.6x10^{-4}$) and *bckdhbl* ($log_2$ fold change=-9.1, p adj.=0.001), that did not meet projection neuron filter criteria. Percentage refers to fraction of all singly-profiled hindbrain vestibular neurons with expression (Methods). Left columns show RNA (green); right columns, merge with projection neurons labeled with *Tg(-6.7Tru.Hcrtr2:GAL4-VP16);Tg(UAS-E1b:Kaede)* (grey). Dashed lines outline the projection nucleus. Cell and transcript expression outside the projection nucleus is removed for visual clarity. All scale bars, 20 μm.

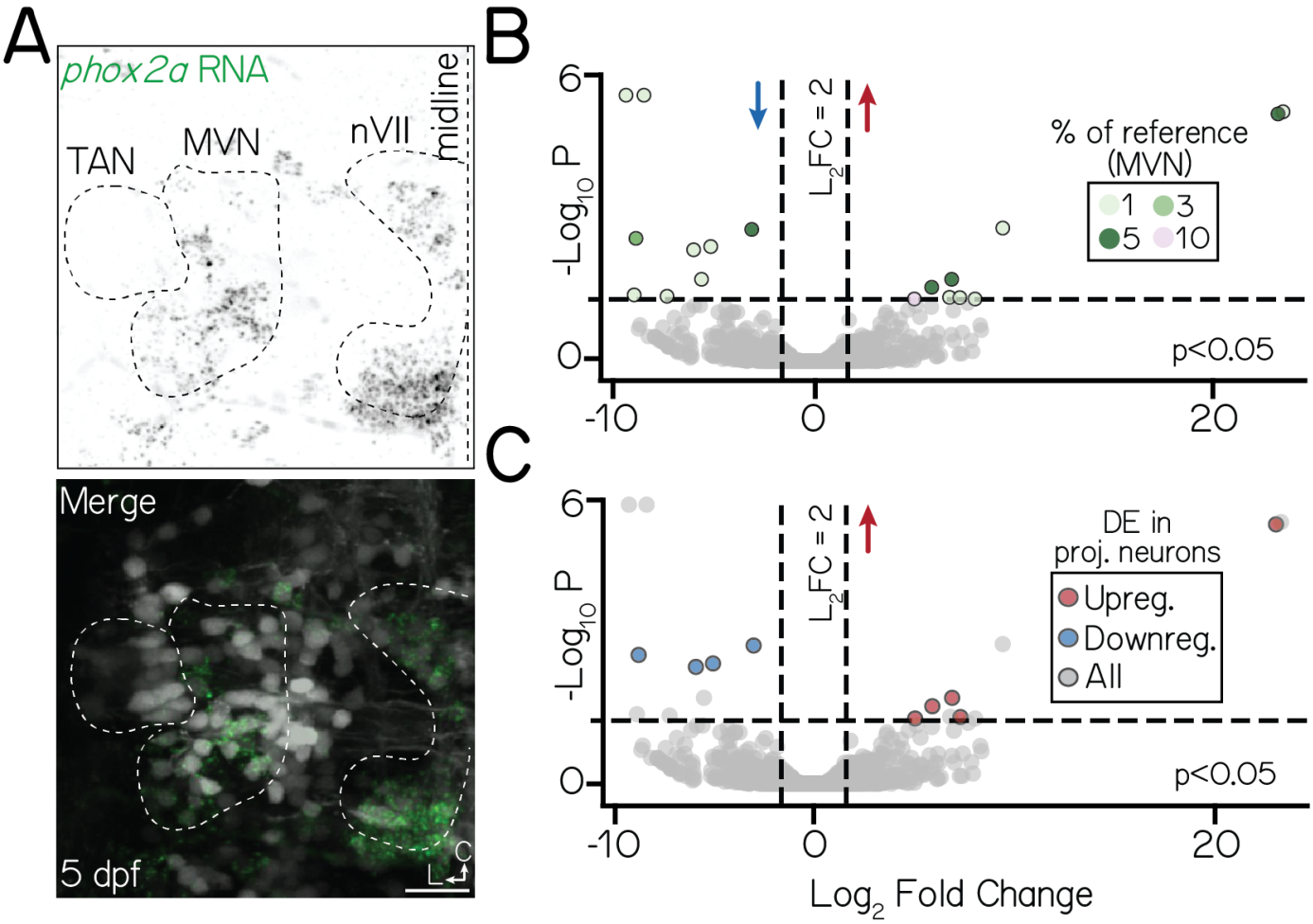


**Figure S7: *phox2a* expression in the medial vestibular nucleus may underscore differential gene expression phenotypes in bulk data.** Associated with Figure 5.

**(A)** Fluorescent *in situ* hybridization against *phox2a* in a 5 dpf larvae (axial view). Top panel shows *phox2a* RNA (green); bottom panel, merge with neurons visualized with *Tg(isl1:GFP);Tg(-6.7Tru.Hcrtr2:GAL4-VP16(;Tg(UAS-E1b:Kaede)* (grey). White dashed lines outline three nuclei of interest: projection neurons in the tangential nucleus (TAN), the medial vestibular nucleus (MVN), and the facial nucleus (nVII). All scale bars, 20 µm.

**(B)** Volanco plot showing differentially expressed genes in *phox2a*-expressing medial vestibular nucleus neurons between control and *phox2a* null larvae at 3 dpf. Dashed lines represent significance cutoffs: horizontal line, p>0.05; vertical line, $Log_2$ Fold Change > 2.0. Each circle is a gene. Genes to the left and right of 0 on the horizontal axis show downregulated and upregulated genes, respectively. Colors indicate percent of reference *phox2a*-expressing medial vestibular neurons (Methods, Figure S4A-Figure S4B) that express a given gene. Grey-colored genes are below both significance thresholds. Data for all differentially expressed candidates in medial vestibular neurons shown in Table 6.

**(C)** Same data as Figure S7B. Color shows genes that are differentially expressed in both medial vestibular nucleus neurons and projection neurons.

| | WT (all) | WT (sampled) | phox2a+/+ | phox2a+/- | phox2a-/- | p val |
|---|---|---|---|---|---|---|
| **Tonic tilt stimuli** | | | | | | |
| n (neurons/fish) | 255/10 | 125/x | 76/5 | 109/6 | 297/16 | |
| % observed (nose-up/nose-down/untuned) | 50/44/7 | 37/54/9 | 40/54/7 | 56/37/7 | 44/50/6 | |
| ΔF/F, nose-up | 1.28±1.23 | 1.27±1.19 | 1.09±1.03 | 1.12±0.90 | 1.02±0.82 | 0.26 |
| ΔF/F, nose-down | 2.01±1.66 | 1.99±1.69 | 1.38±0.91 | 1.98±1.61 | 2.07±1.48 | 0.16 |
| directional tuning strength, nose-up | 0.84±0.28 | 0.83±0.30 | 0.87±0.26 | 0.81±0.28 | 0.81±0.29 | 0.70 |
| directional tuning strength, nose-down | 0.72±0.30 | 0.72±0.31 | 0.73±0.31 | 0.77±0.30 | 0.68±0.29 | 0.54 |
| **Impulse stimuli** | | | | | | |
| n (neurons/fish) | 255/10 | 125/x | 76/5 | 109/6 | 297/16 | |
| % observed (responsive/unresponsive) | 58/42 | 57/43 | 57/43 | 60/39 | 70/30 | |
| ΔF/F | 0.41±0.46 | 0.33±0.28 | 0.29±0.29 | 0.22±0.16 | 0.32±0.28 | 1.0E-05 |
| directional tuning strength | 0.08±0.36 | 0.10±0.38 | 0.003±0.41 | 0.07±0.48 | 0.07±0.41 | 0.64 |
| **Multiple comparisons** | **genotype** | | **p val** | **Cohen's d** | | |
| ΔF/F to impulses | WT to sampled | | p=0.13 | 0.21 | | |
| | WT to +/+ | | p=0.04 | 0.27 | | |
| | WT to +/- | | p=3.8E-06 | 0.48 | | |
| | WT to -/- | | p=0.006 | 0.24 | | |
| | +/+ to +/- | | p=0.47 | 0.34 | | |
| | +/+ to -/- | | p=0.89 | 0.11 | | |
| | +/- to -/- | | p=0.02 | 0.49 | | |

**Table 1: Statistical comparisons of tilt responses across genotypes.** WT (sampled) refers to an n=125 neuron subset, sampled with replacement from a reference dataset of wildtype projection neurons. Data shown is mean/standard deviation unless otherwise noted. p val generated from a one-way ANOVA with multiple comparisons. Associated with Figure 2 and Figure 3.

| | WT (all) | WT (sampled) | phox2a+/+ | phox2a+/- | phox2a-/- | p val |
|---|---|---|---|---|---|---|
| **Tonic tilt stimuli** | | | | | | |
| *nose-down* | | | | | | |
| n (cells/fish) | 111/10 | 51/x | 41/5 | 40/6 | 147/16 | |
| dorsoventral | 20.0±8.4 | 25.0±8.4 | 15.0±9.0 | 25.0±8.7 | 20.0±9.1 | 0.03 |
| mediolateral | 17.4±6.0 | 17.6±6.5 | 19.3±6.6 | 15.3±5.6 | 16.8±6.6 | 0.15 |
| rostrocaudal | 16.8±9.6 | 16.5±9.6 | 19.5±9.6 | 16.1±10.4 | 18.2±9.6 | 0.49 |
| global organization | | | | | | 0.09 |
| *nose-up* | | | | | | |
| n (cells/fish) | 111/10 | 51/x | 41/5 | 40/6 | 147/16 | |
| dorsoventral | 30.0±10.3 | 25.0±10.8 | 27.5±10.9 | 25.0±10.4 | 30.0±10.5 | 0.67 |
| mediolateral | 14.9±7.1 | 15.1±5.9 | 16.7±7.0 | 18.6±9.8 | 13.2±7.2 | 9.6E-06 |
| rostrocaudal | 16.1±9.8 | 16.7±10.4 | 12.5±10.7 | 14.8±10.4 | 14.8±10.7 | 0.51 |
| global organization | | | | | | 2.7E-07 |
| **Multiple comparisons** | **genotype** | | **p val** | **Cohen's d** | | |
| dorsoventral, nose-down | WT to sampled | | 0.86 | 0.17 | | |
| | WT to +/+ | | 0.54 | 0.29 | | |
| | WT to +/- | | 0.96 | 0.13 | | |
| | WT to -/- | | 0.08 | 0.34 | | |
| | +/+ to +/- | | 0.35 | 0.41 | | |
| | +/+ to -/- | | 0.99 | 0.05 | | |
| | +/- to -/- | | 0.07 | 0.45 | | |
| mediolateral, nose-up | WT to sampled | | 0.91 | 0.03 | | |
| | WT to +/+ | | 0.57 | 0.35 | | |
| | WT to +/- | | 0.006 | 0.57 | | |
| | WT to -/- | | 0.69 | 0.20 | | |
| | +/+ to +/- | | 0.74 | 0.23 | | |
| | +/+ to -/- | | 0.09 | 0.55 | | |
| | +/- to -/- | | 5.4E-06 | 0.74 | | |
| **Impulse stimuli** | | | | | | |
| n (responsive) | 148/10 | 138/n | 43/5 | 55/5 | 214/16 | |
| dorsoventral | 20.0±9.8 | 20.0±10.1 | 20.0±10.7 | 20.0±10.9 | 20.0±10.3 | 0.57 |
| mediolateral | 19.0±5.9 | 16.1±6.8 | 16.7±8.6 | 20.4±7.2 | 19.8±5.8 | 0.003 |
| rostrocaudal | 21.9±9.9 | 17.3±9.8 | 15.4±9.1 | 13.0±9.9 | 22.0±9.5 | 2.9E-05 |
| global organization | | | | | | 1.2E-0.9 |
| **Multiple comparisons** | **genotype** | | **p val** | **Cohen's d** | | |
| mediolateral, responsive | WT to sampled | | 0.99 | 0.002 | | |
| | WT to +/+ | | 0.32 | 0.37 | | |
| | WT to +/- | | 9.82 | 0.17 | | |
| | WT to -/- | | 0.33 | 0.23 | | |
| | +/+ to +/- | | 0.91 | 0.14 | | |
| | +/+ to -/- | | 0.007 | 0.55 | | |
| | +/- to -/- | | 0.05 | 0.37 | | |
| rostrocaudal, responsive | WT to sampled | | 0.98 | 0.37 | | |
| | WT to +/+ | | 0.12 | 0.29 | | |
| | WT to +/- | | 0.001 | 0.53 | | |
| | WT to -/- | | 0.07 | 0.10 | | |
| | +/+ to +/- | | 0.90 | 0.72 | | |
| | +/+ to -/- | | 0.95 | 0.33 | | |
| | +/- to -/- | | 0.23 | 0.21 | | |

**Table 2: Statistical comparisons of projection neuron topography across genotypes.** WT (sampled) refers to an n=125 neuron subset, sampled with replacement from a reference dataset of wildtype projection neurons. Data shown is the median/standard deviation distance from the ventro-lateral and rostral edges of the tangential nucleus (total size: 40 µm across each spatial axis). p val from one-way analysis of variance (individual spatial axes) or multivariate analysis of variance (global organization), respectively.

| Gene | % of projection neurons with expression | $Log_2$ fold change | p adjusted |
|---|---|---|---|
| **Upregulated** | | | |
| ** # itga9* | 1.9 | 23.0 | 3.9E-06 |
| *si:dkey-54n8.2* | 1.3 | 9.6 | 0.007 |
| *myof* | 1.3 | -8.3 | 0.010 |
| *gbe1a* | 1.9 | 7.0 | 0.01 |
| *# dysf* | 1.9 | 6.9 | 0.016 |
| ** # twf1b* | 2.5 | 5.9 | 0.024 |
| *cers3a* | 2.5 | 9.2 | 0.025 |
| *asip2b* | 1.3 | 8.7 | 0.032 |
| *# pole* | 1.3 | 7.3 | 0.041 |
| *abtb2a* | 3.1 | 4.7 | 0.041 |
| ** # p4hb* | 6.3 | 5.1 | 0.044 |
| *postnb* | 3.8 | 10.1 | 0.044 |
| *fhdc3* | 2.5 | 4.5 | 0.044 |
| **Downregulated** | | | |
| *msmo1* | 1.3 | -8.3 | 8.4E-06 |
| **rxfp2a* | 4.4 | -8.5 | 1.1E-05 |
| *si:ch73-204p21.2* | 1.3 | -9.9 | 2.2E-04 |
| *tsta3* | 0.0 | -6.6 | 6.8E-04 |
| ** # satb1a* | 8.2 | -3.0 | 0.001 |
| *# polrmt* | 1.9 | -8.7 | 0.002 |
| *# znf975* | 1.3 | -5.0 | 0.003 |
| *# phldb1a* | 3.1 | -5.8 | 0.004 |
| *asns* | 2.5 | -7.8 | 0.032 |
| *nr1i2* | 1.9 | -5.5 | 0.039 |
| **Control** | | | |
| *evx2* | 36.4 | 0.46 | 0.99 |
| *myt1la* | 80.5 | 2.6 | 0.44 |

**Table 3: Differentially expressed genes in projection neurons.** Star indicates a gene was evaluated using fluorescent *in situ* hybridization. # symbol indicates a gene was also differentially expressed in adjacent *phox2a*-expressing medial vestibular neurons (see Figure S7). "% of projection neurons with expression" refers to detection in a filtered subset of projection neurons from a single-cell reference atlas of neurons labeled in *Tg(-6.7Tru.Hcrtr2:GAL4-VP16);Tg(UAS-E1b:Kaede)* (Methods, Figure S4). Genes sorted by p adjusted value. Data associated with Figure 5.

| Gene | % of unfiltered 10x neurons with expression | % of projection neurons |
|---|---|---|
| *ints5* | 23.2 | 15.1 |
| *stmn1b* | 78.6 | 78.6 |
| *sox4a* | 6.5 | 3.1 |
| *basp1* | 61.4 | 62.9 |
| *hmgb3a* | 68.2 | 69.8 |
| *ptmaa* | 84.5 | 77.4 |
| *gapdhs* | 28.9 | 30.2 |
| *pnrc2* | 81.3 | 78.6 |
| *snap25a* | 65.7 | 78.0 |
| *gpm6ab* | 81.1 | 78.6 |
| *calm3b* | 0.0 | 0.0 |
| *marcksl1b* | 88.8 | 86.2 |
| *tuba1c* | 59.9 | 54.7 |
| *cd81a* | 43.3 | 49.7 |
| *meis1b* | 87.9 | 87.4 |
| *rtn1a* | 73.4 | 74.8 |
| *elavl3* | 87.1 | 82.4 |
| *hmgb1b* | 57.2 | 49.7 |
| *ptmab* | 80.7 | 73.6 |
| *zc4h2* | 56.9 | 58.5 |
| *meis2b* | 57.1 | 49.7 |
| *slc25a5* | 51.4 | 55.3 |
| *mab21l2* | 62.7 | 68.6 |
| *h3f3c* | 69.1 | 61.6 |
| *rtn1b* | 36.4 | 33.3 |
| *elavl4* | 78.7 | 67.3 |
| *gng3* | 37.2 | 42.8 |
| *pik3r3b* | 77.4 | 83.6 |
| *tubb5* | 25.3 | 25.2 |
| *histh1l* | 61.0 | 62.9 |
| *serinc1* | 51.9 | 59.1 |
| *ckbb* | 23.5 | 30.8 |
| *oaz1a* | 43.5 | 49.7 |
| *oaz1b* | 36.9 | 38.4 |
| *actb1* | 23.6 | 28.3 |
| *ywhaba* | 36.2 | 40.9 |
| *ywhag2* | 36.2 | 50.9 |
| *si:ch211-222l21.1* | 73.8 | 63.5 |
| *si:dkey-276j7.1* | 45.8 | 56.0 |
| *aldocb* | 19.3 | 17.6 |
| *actb2* | 27.0 | 30.8 |
| *tmem59l* | 39.8 | 56.6 |
| *calm2b* | 37.9 | 47.2 |
| *hmgn6* | 73.6 | 65.4 |
| *h2afx1* | 59.6 | 53.5 |
| *cd99l2* | 32.4 | 36.5 |
| *cirbpb* | 77.8 | 73.6 |
| *ppdpfb* | 74.5 | 65.4 |
| *stxbp1a* | 52.3 | 66.0 |
| | | |
| **Control** | | |
| *evx2* | 33.8 | 36.4 |

**Table 4: Top 50 expressed genes in an unfiltered bulk RNA sequencing dataset of *phox2a* siblings.** "% of unfiltered 10x neurons" refers to gene detection in a single-cell atlas of neurons labeled in *Tg(-6.7Tru.Hcrtr2:GAL4-VP16);Tg(UAS-E1b:Kaede)* (n=1,468 neurons). "% of projection neurons" refers to gene detection in a subset of the single-cell atlas containing projection neurons in the tangential nucleus (n=159 neurons). Data associated with Figure 5.

| Gene | % of unfiltered 10x neurons with expression | Putative origin | $Log_2$ fold change | p adjusted |
|---|---|---|---|---|
| **Upregulated** | | | | |
| *macc1* | 0.1 | r4-6 | 24.0 | 3.2E-06 |
| *CR559941.1* | 0.0 | | 23.7 | 3.4E-06 |
| *si:dkey-65b12.6* | 0.0 | | 23.5 | 3.4E-06 |
| *si:ch73-106n3.2* | 0.1 | | 23.5 | 3.4E-06 |
| *mcm10* | 0.1 | MNs | 23.4 | 3.4E-06 |
| *si:ch211-244o22.2* | 0.5 | r4-6 | 23.4 | 3.4E-06 |
| *dre-mir-10a* | 0.0 | | 23.3 | 3.5E-06 |
| *itga4* | 0.3 | r5-6 (inhibitory) | 23.2 | 3.5E-06 |
| *si:dkeyp-87d8.8* | 0.0 | | 23.2 | 3.6E-06 |
| *arsj* | 0.5 | MNs | 23.0 | 3.9E-06 |
| *tlr1* | 0.0 | | 23.0 | 3.9E-06 |
| ** % itga9* | 2.3 | r4-7 | 23.0 | 3.9E-06 |
| *otofb* | 0.5 | r4-6 | 9.1 | 1.4E-05 |
| *myo7ba* | 0.4 | r4-7 | 9.8 | 1.0E-04 |
| *zfand1* | 0.1 | MNs | 9.0 | 1.5E-04 |
| *% slc22a7a* | 0.7 | r4-7 | 10.2 | 1.5E-04 |
| *agrp* | 0.0 | | 13.4 | 4.1E-04 |
| *si:dkey-46i9.6* | 0.1 | r5-7 | 7.7 | 6.8E-04 |
| *muc2.2* | 0.0 | | 9.4 | 6.9E-04 |
| *cd37* | 0.0 | | 9.1 | 9.8E-04 |
| *musk* | 0.3 | r4-6 | 9.4 | 1.2E-03 |
| *mcamb* | 0.2 | r5-7 | 8.3 | 2.7E-03 |
| *ppp1r42* | 0.5 | r5-6 (inhibitory) | 7.9 | 3.1E-03 |
| *CR677513.1* | 0.0 | | 9.9 | 3.5E-03 |
| **Downregulated** | | | | |
| ** % satb1a* | 7.9 | r4-7 (inc. inhib), MNs | -8.6 | 1.0E-06 |
| **znf975* | 0.7 | r4-6 | -8.3 | 1.5E-06 |
| *phldb1a* | 0.6 | r5-7 (inc. inhib) | -9.2 | 1.5E-06 |
| *TSTA3* | 0.0 | | -9.7 | 3.4E-06 |
| *si:dkey-24p1.6* | 0.0 | | -8.3 | 8.4E-06 |
| *si:dkey-77f5.14* | 0.2 | r5-7 | -8.5 | 1.1E-05 |
| *tha1* | 0.1 | MVN | -10.3 | 2.1E-05 |
| *serpinh2* | 0.5 | r4-6 | -9.0 | 3.7E-05 |
| *ghrh* | 0.3 | r4-7 | -9.5 | 6.9E-05 |
| *asah1b* | 0.8 | r4-7 | -7.8 | 9.9E-05 |
| *msmo1* | 0.9 | r5-7, inc. inhib | -8.9 | 1.1E-04 |
| *tagln2* | 0.3 | glia | -8.4 | 2.2E-04 |
| *zgc:174863* | 0.1 | MNs | -9.9 | 2.2E-04 |
| ** % rxfp2a* | 3.2 | r4-7, inc. inhib | -6.6 | 6.8E-04 |
| *bmp4* | 0.7 | r4-7 | -6.8 | 6.8E-04 |
| *cfl1l* | 0.1 | r4-6 | -8.4 | 6.8E-04 |
| ** polrmt* | 4.2 | r4-7, inc. inhib | -8.8 | 6.9E-04 |
| *anxa2a* | 0.6 | r4-7 | -3.0 | 1.3E-03 |
| *galr1a* | 0.3 | MVN | -9.1 | 1.4E-03 |
| *selenow2b* | 0.1 | | -8.0 | 1.8E-03 |
| *% bckdhbl* | 1.4 | r4-7, glia, MNs | -8.7 | 2.1E-03 |
| *boka* | 0.5 | r5-7 | -8.6 | 2.9E-03 |
| *cyldb* | 0.2 | r4-7 | -7.9 | 3.0E-03 |
| *pon2* | 0.6 | r4-7, glia, MNs | -5.0 | 3.1E-03 |
| *si:ch73-204p21.2* | 0.3 | r5-7, inc. inhib | -8.2 | 3.5E-03 |
| *and2* | 0.1 | r4-6 | -5.8 | 3.7E-03 |
| **Control** | | | | |
| *evx2* | 33.8 | r4-7 | 0.46 | 0.99 |

**Table 5: Top 50 differentially expressed genes in an unfiltered bulk RNA sequencing dataset of *phox2a* siblings and null mutants.** One star indicates a gene was retained in a filtered subset of projection neurons; %, evaluated using fluorescent *in situ* hybridization. "% of unfiltered 10x neurons" refers to gene detection in an unfiltered single-cell reference atlas of neurons labeled in *Tg(-6.7Tru.Hcrtr2:GAL4-VP16);Tg(UAS-E1b:Kaede)* (n=1,468 neurons). Putative origin inferred from gene expression in the annotated 10x dataset (Methods, Figure S4)). Genes sorted by p adjusted value. Data associated with Figure 5.

| Gene | % of medial vestibular neurons | % of projection neurons | $Log_2$ fold change | p adjusted |
|---|---|---|---|---|
| **Upregulated** | | | | |
| *itga4* | 2.2 | 0.6 | 23.2 | 3.5E-06 |
| * # *itga9* | 6.7 | 1.9 | 23.0 | 3.9E-06 |
| *musk* | 2.2 | 0.6 | 9.4 | 0.001 |
| # *dysf* | 6.7 | 1.9 | 6.9 | 0.016 |
| * # *twf1b* | 8.9 | 1.9 | 5.9 | 0.024 |
| *gabrr2a* | 2.2 | 2.5 | 6.8 | 0.040 |
| # *pole* | 2.2 | 0.0 | 7.3 | 0.041 |
| * # *p4hb* | 15.6 | 1.3 | 5.1 | 0.044 |
| *col27a1b* | 2.2 | 0.6 | 8.0 | 0.044 |
| **Downregulated** | | | | |
| *asah1b* | 2.2 | 0.0 | -8.3 | 1.5E-06 |
| *boka* | 2.2 | 0.0 | -9.2 | 1.5E-06 |
| * # *satb1a* | 6.7 | 8.2 | -3.0 | 0.001 |
| # *polrmt* | 4.4 | 1.9 | -8.7 | 0.002 |
| # *znf975* | 2.2 | 1.3 | -5.0 | 0.003 |
| # *phldb1a* | 2.2 | 3.1 | -5.8 | 0.004 |
| *fosl1a* | 2.2 | 0.0 | -5.4 | 0.016 |
| *pitpnaa* | 2.2 | 0.0 | -8.8 | 0.036 |
| *sgpp1* | 2.2 | 0.6 | -7.1 | 0.038 |

**Table 6: Differentially expressed genes in *phox2a*-expressing medial vestibular neurons**. Star indicates a gene was evaluated in projection neurons using fluorescent *in situ* hybridization. # indicates a gene was significantly differentially expressed in projection neurons. "% of medial vestibular neurons" refers to detection in a subset of *phox2a*-expressing medial vestibular neurons in a single-cell reference atlas (Methods, Figure S4). "% of projection neurons with expression" refers to detection in a filtered subset of projection neurons. Gene sorted by p adjusted value. Data associated with Figure 5

| REAGENT or RESOURCE | SOURCE | IDENTIFIER |
|---|---|---|
| **Chemicals, peptides, and recombinant proteins** | | |
| Tween | Fisher Scientific | BP337-100 |
| 32% paraformaldehyde | Electron Microscopy Sciences | 15714 |
| Proteinase K | ThermoFisher Scientific | 25530049 |
| Papain | Worthington Biochemical | LK003178 |
| Hanks Buffered Salt Solution (HBSS) | ThermoFisher Scientific | 14170112 |
| Earl's Buffered Salt Solution (EBSS) | ThermoFisher Scientific | 24010043 |
| DNAse | Worthington Biochemical | LK003172 |
| DAPI | Invitrogen | D1306 |
| L15 Medium | ThermoFisher Scientific | 11415064 |
| Fetal bovine serum, qualified, triple-filtered | ThermoFisher Scientific | A3160501 |
| Collagenase Type 1A | Sigma Aldrich | C9891-500MG |
| Low melting point agarose | ThermoFisher Scientific | 16520 |
| Ethyl-3-aminobenzoic acid ethyl ester (MESAB) | Sigma Aldrich | E10521 |
| Pancuronium bromide | Sigma Aldrich | P1918 |
| **Critical commercial assays** | | |
| *in situ* hybridization chain reaction v3.0 (HCR) | Molecular Instruments | N/A |
| RNAqueous Micro Total RNA Isolation Kit | ThermoFisher Scientific | AM1931 |
| MEGAshortscript T7 Transcription Kit | ThermoFisher Scientific | AM1354 |
| QiaQUICK PCR Purification Kit | Qiagen | 28104 |
| EnGen Spy Cas9 NLS | New England Biolabs | M0646T |
| **Deposited data** | | |
| Raw and analyzed calcium imaging data | This study | DOI: 10.17605/OSF.IO/93V6E |
| Raw and analyzed 10x Genomics scRNA-seq datasets | This study | GEO: GSE254346 |
| Raw and analyzed bulk RNA seq datasets | This study | GEO: GSE254345 |
| **Experimental models: Organisms/strains** | | |
| *Tg(-6.7Tru.Hcrtr2:GAL4-VP16)* | [25,49] | ZFIN: ZDB-TGCONSTRCT-151028-8 |
| *Tg(UAS-E1b:Kaede)* | [48] | ZFIN: ZDB-TGCONSTRCT-070314-1 |
| *Tg(isl1:GFP)* | [40] | ZFIN: ZDB-ALT-030919-2 |
| *Tg(UAS:GCaMP6s)* | [42] | ZFIN: ZDB-TGCONSTRCT-140811-3 |
| *phox2a*$^{d22}$ | This study | N/A |
| *phox2a*$^{d19}$ | This study | N/A |
| *phox2a*$^{i2}$ | This study | N/A |
| **Oligonucleotides** | | |
| *phox2a* forward primer (5-CAGCCAGAGCAACGGCTTCC-3) | Sigma Aldrich | N/A |
| *phox2a* reverse primer (5-AAGCCGACAACAGTGTGTGTGTAA-3) | Sigma Aldrich | N/A |
| *phox2a* guide 1 (5-CTCGCCACCGCCAGCTGCAC-3) | Sigma Aldrich | N/A |
| *phox2a* guide 2 (5-CTCCGGCTTCAGCTCCGGCC-3) | Sigma Aldrich | N/A |
| HCR probes | Integrated DNA Technologies | N/A |
| **Software and algorithms** | | |
| Fiji/ImageJ | [124] | RRID: SCR_02285 |
| Adobe Illustrator (2021) | Adobe | RRID: SCR_010279 |
| Matlab 2020b | Mathworks | RRID: SCR_001622 |
| Seurat v4 | [133] | https://satijalab.org/seurat |
| CRISPR Guide RNA Design Tool | Benchling | https://benchling.com/crispr |
| **Other** | | |
| 20 micron cell strainer | pluriSelect | 431002060 |
| SH800z 100 micron sorting chip | Sony | LE-C3210 |

**Table 7:** Key Resources Table (associated with Methods).